scientific reports

Check for updates

OPEN

Process optimization and modeling research for the defluoridation of water using a novel adsorbent of cellulose and hydroxyapatite nanocomposite

Samuel Latebo Majamo[1]✉, Temesgen Abeto Amibo[2,3], Bereket Mamo Gebremeskel[4] & Donata Konopacka-Łyskawa[2]

According to world health organization fluoride ion concentration in the drinking water greater than 1.5 mg/L results in humans healthy risks. In this research, a cellulose/hydroxyapatite nanocomposite was produced and used for fluoride ions removal from water by adsorption. To synthesize the nanocomposite, cellulose of African alpine bamboo (*Yushuania alpina*) and (ii) hydroxyapatite of chicken eggshells were used. The adsorbent characteristics were determined based on dynamic light scattering, Brunauer-Emmett-Teller, scanning electron microscopy, Fourier transform infrared spectroscopy, x-ray diffraction, thermogravimetric analysis and derivative thermogravimetric analysis. Adsorption experiments were designed by the central composite design approach. The influence of an adsorbent dose (0.075–1.75 g/L), pH (5–9), contact time (40–80 min) and initial fluoride ion concentration (20–40 mg/L) were investigated. The highest adsorption capacity of the adsorbent was 23.02 mg/g. The highest removal efficiency of 98.68% was attained by employing dosage of 1.43 g/L for 77 min, at a pH of 5.24, and with an initial concentration of 24.43 mg/L. Thermodynamic analysis shows that the process is spontaneous and endothermic, as confirmed by the positive values of ΔH° and ΔS°, and the negative values of ΔG°. The adsorption process can be described the pseudo-second-order kinetic model and the Langmuir isotherm. The study showed that the cellulose/hydroxyapatite nanocomposite is an environmentally friendly and effective adsorbent for fluoride ion removal.

Keywords Cellulose/hydroxyapatite nanocomposite, Defluoridation, RSM, Kinetics, Isotherm, Thermodynamics

Water is the most essential and primary need of all living organisms[1,2]. The readily available source of freshwater is groundwater. Purifying water from any contaminants is a crucial task[3]. One of the inorganic pollutants in groundwater is fluoride[4,5]. Minerals such as fluorite, biotite, and topaz found in rocks gradually disintegrate, causing fluoride pollution in groundwater. Fluoride possesses certain physiological features that are highly relevant to human health and well-being. Fluoride plays a significant role in the mineralization of hard tissues. Low-dose fluoride improves the skeletal system by enlarging apatite crystals and decreasing their solubility[6]. On the other hand, the World Health Organization (WHO) has warned that consuming water containing fluoride levels over 1.5 mg/L poses a risk to human health. Halogen elements in water provide environmental issues, since fluoride inhibits tooth decay while also leading to skeletal fluorosis, nerve injury, and bone demineralization, mostly through use of drinking water and industrial effluent[7,8]. A recent study investigated the health hazards linked to prolonged exposure to non-skeletal fluorosis, which can negatively impact several bodily systems, including the kidney, liver, endocrine glands, neurological system, metabolism, cardiovascular system, reproductive system, and structural integrity[9].

[1]Department of Chemical Engineering, College of Engineering and Technology, Wachemo University, Hossana, Ethiopia. [2]Department of Process Engineering and Chemical Technology, Faculty of Chemistry, Gdansk University of Technology, Narutowicza 11/12, Gdansk 80-233, Poland. [3]School of Chemical En`gineering, Jimma Institute of Technology, Jimma University, P.O. Box-378, Jimma, Ethiopia. [4]Institute of Soil Mechanics and Rock Mechanics, Karlsruhe Institute of Technology, 76-133 Karlsruhe, Germany. ✉email: Samuel.latebo23@gmail.com

Therefore, the most efficient, cost-effective, and environmentally friendly technique for eliminating excess fluoride from water is an important challenge. Various technologies such as coagulation-precipitation, nano-filtration, reverse osmosis, electro-dialysis, membrane separation, ion exchange, adsorption, and electrodialysis are proposed to remove fluoride ions from water[7,10]. The Nalgonda method, a regularly used water treatment technology, utilizes coagulation-precipitation, leading to higher operational costs and relatively poor water quality test results[6]. Membrane technology is effective but expensive and may eliminate vital minerals like magnesium, calcium, and potassium. Furthermore, the ion exchange process generates waste and it cost is high, although this method is very efficient. However, the adsorption technique is advantageous due to its cost-effectiveness, high efficiency, eco-friendliness, and suitability for large-scale use[11].

A variety of adsorbents such as natural and activated coal, chitosan-based mesoporous alumina, lanthanum-impregnated activated alumina, magnesia-amended activated alumina, and others have been developed and utilized to defluoridate water[12]. Additionally, metal such as oxide nanoparticles, including iron, aluminum, titanium, cerium, and manganese, were used to achieve the highest possible defluoridation efficiency[13]. Aside from these materials being expensive, some can have harmful side effects due to metals leaching into the reaction medium[13].

Recently, hydroxyapatite (HAp), $Ca_5(PO_4)_3(OH)$, can be used as an adsorbent of fluoride ions. The advantages of Hap, as a sorption material, are outstanding stability, non-toxicity, cost-effectiveness, and recyclability. Yapo et al.[14] proposed fluoride adsorption by modified Hap from bivalve shells. The specific surface area was 249.3 m^2/g and the adsorption capacity of fluoride ions was 4.517 mg/g when the sorbent dosage was 5 g/L. The tested adsorbent allowed the removal of fluoride ions from water to the level recommended by WHO for drinking water. These results showed the great potential of this material as an adsorbent, however, testing was limited to examining the effect of fluoride ion concentration on the adsorption amount and determining the kinetics and thermodynamic parameters of the process. Despite extensive research on the utilization of hydroxyapatite for the fluoride ions removal, only some studies achieved a sorption capacity of F^- ions higher than 10 mg/L[15]. Also in the literature, little information is on the adsorption optimization of these ions using hydroxyapatite. In the case of process optimization for synthetic HAp, the most favorable result was the removal of approximately 86% of F- ions, their concentration in the solution was 20 mg/L and the adsorbent dose was 0.28 g[16]. For composite adsorbents, the reported sorption capacity values rarely reached above 10 mg/L, and the removal efficiency of F^- ions was efficient for low concentrations of this pollutant[15].

In order to effectively remove fluoride ions from water, this study presents a cellulose/hydroxyapatite (HAp) nanocomposite made from sustainable resources, especially chicken eggshells and African alpine bamboo. In order to enhance fluoride removal effectiveness, the study uses the Central Composite Design (CCD) technique to optimize key adsorption parameters, including adsorbent dosage, pH, contact time, and initial fluoride concentration. This paper provides a novel method for improving fluoride removal by investigating the adsorption isotherm, kinetics, and thermodynamics, outperforming earlier sorption capabilities documented in the literature. Past studies have demonstrated cellulose is a suitable component as a backbone in composite formation to remove fluoride from water[17]. Numerical optimization was performed to indicate the optimal conditions for fluoride ion removal. Furthermore, the sorption properties of the obtained new nanocomposite, i.e., the adsorption isotherm of fluoride ions, kinetics, and thermodynamics characterizing the removal of this pollutant were determined.

Materials and methods

Materials

African alpine bamboo (*Yushania alpine) waste* was collected from local area of Doyogena woreda, central Ethiopian region, Ethiopia and utilized for cellulose extraction. In addition, discarded chicken eggshell was used for synthesis of HAp.

Chemicals

Acetic acid CH_3COOH (99.6% pure), sulfuric acid H_2SO_4 (98%), hydrochloric acid HCl (37%), sodium hydroxide NaOH (99% pure), ethanol C_2H_5OH (99.9%), hydrogen peroxide H_2O_2 (30%), phosphoric acid H_3PO_4 (99%), calcium chloride $CaCl_2$ (97%), sodium dihydrogen phosphate dehydrate $NaH_2PO_4.2H_2O$ (99%), sodium fluoride NaF (98%) and ammonium hydroxide NH_4OH (28%) were purchase from Chirico's Chemical Suppliers in Addis Ababa, Ethiopia. Distilled water was used throughout experiments. All chemicals used in this study have been analytical graded and utilized without purification.

Methods

Cellulose extraction

The bamboo was cleaned by washing it three times with distilled water to remove any impurities. Then, the purified lignocellulosic material was dehydrated for 24 h at 105 °C in an oven using the method described in[18]. The pre-prepared bamboo sample was pulverized in a steel ball mill and sifted through a 60-mesh screen. The resulting bamboo powder with a particle size of less than 250 µm was stored. To produce improved cellulose with lower amounts of hemicellulose and lignin, which contain harmful compounds such as phenolic aldehydes and acids, the optimal conditions for enhancing cellulose extraction provided by Majamo et al.[17] were used with very few adjustments. The pretreatment was performed using a mixture of two acids (H_2SO_4 and CH_3COOH) in a 0.44 ratio with a concentration of 2.3% for 83 min at 105 °C. The pretreated material was subjected into bleaching process. It was processed with 4% NaOH and then treated with 7.5% H_2O_2. The bleached material was placed in a water bath set at 70 °C and stirred at 200 rpm for 30 min. After the end of designated period, it was cooled to room temperature and repeatedly washed with hot distilled water to eliminate any residual contaminants and lignin. Then it was subsequently dehydrated at 105 °C for 30 min and was ready for further use.

Hydroxyapatite synthesis

The HAp was produced using a process described in the references[19,20]. The chicken eggshell was initially processed to eliminate contaminants. It was repeatedly washed with distilled water and then, boiled to remove the inner membrane. The purified material was then dehydrated in an oven at 100 °C for 12 h to eliminate volatile impurities. The dried solid was ground into a fine powder consists of $CaCO_3$. $CaCO_3$ was converted into CaO by calcining it in a muffle furnace at 900 °C for 2 h. Then, it was cooled to room temperature[20]. To make 1 M $Ca(OH)_2$ solution, calcined CaO was dissolved in distilled water and heated in water bath of 40 °C[20]. Then, 0.6 M H_3PO_4 was added drop by drop. The pH of sample was raised to 9 by adding 28% NH_4OH solution. The resulting mixture was stirred for 2 h and then it was placed at room temperature for 24 h to form a precipitate. The solid product was separated by centrifuge. After drying the isolated precipitate at 100 °C for 12 h to remove solvents, the material was heated at 900 °C with a rate of 10 °C per hour for 2 h to produce Hap[20]. The overall reaction occurring during the synthesis of HAp can be written as:

$$10Ca(OH)_2 + 6H_3PO_4 \rightarrow Ca_{10}(PO_4)_6(OH)_2 + H_2O \quad (1)$$

Cellulose/hydroxyapatite synthesis

The cellulose/HAp nanocomposite was synthesized using the technique outlined in[21]. 4.8 g of urea and 2.8 g of NaOH were dissolved in 32.4 mL of deionized. Following that, at the ambient temperature, 1.0 g of cellulose was slowly introduced into the aqueous solution while agitated with a magnetic stirrer. The solution was then cooled at -12 °C for 12 h. Subsequently, 0.111 g of calcium chloride ($CaCl_2$) and 0.093 g of sodium dihydrogen phosphate ($NaH_2PO_4.2H_2O$) with a molar ratio of $Ca/P = 1.67$ were added to the cellulose solution. 0.7 g of Hap was introduced into the resulting solution. Hence, the Hap/cellulose mass ratio was set at 70%, optimum mass ratio as described in[21]. At this mass ratio, mineral such as byproduct - portlandite cannot exist[21]. Then, the suspended sample was sonicated using a sonicator (Q55 model, Qsonica) at 55 watts at a frequency of 20 kHz, powered by 110 volts at room temperature. After 30 min, the product underwent centrifugation, was washed with deionized water, and was subsequently freeze-dried in a deep freeze-dryer (model: PTB-292, India).

Adsorbent characterization

The particle size distribution of cellulose, Hap, and cellulose/HAp nanocomposite was analyzed by Zeta DLS (Sizer Nano series, ZE3600, Malvern). The data was collected in Malvern Zeta Sizer software. The surface morphology of cellulose, HAp, and cellulose/HAp nanocomposite before and after adsorption wwas performed using SEM (FEI INSPECT F50). The device was operated with an accelerating voltage of 15 kV. The Brunauer-Emmett-Teller (BET) method was used to determine the specific surface area, pore size, and pore volume of the tested materials. The BET (SA-9600 Series, Horiba Instrument, Inc.) was operated at 77 K. The samples were degassed at 100 °C for 2 h under N_2 gas with a relative pressure range of 0.05–0.30. FTIR (L1600300 Spectrum TWO UTA) was used to identify the functional groups and characteristic bonds in the cellulose, HAp, and nanocomposite. FTIR spectra were taken in the wavelength range of 4000 –400 cm^{-1} at a resolution of 4 cm^{-1}, with KBr as a reference material. The XRD (XRD-7000, SHIMADZU) device was used to analyze the amorphous and crystallographic characteristics of cellulose, HAp, and cellulose/ HAp nanocomposite. The analysis was conducted at an accelerating voltage of 40 kV and a current of 30 mA within a scanning range of 10–85 °C. DTG (DTG-60 H, SHIMADZU) was used to analyze the thermal properties of cellulose, HAp, and cellulose/HAp nanocomposite. The heating was conducted from an initial temperature of 29 °C to a final temperature of 801 °C in a nitrogen environment with a flow rate of 50 mL/min.

Adsorption experiment

The experiment was designed using Design Expert software version 11. The CCD approach was used to test four process variables (dose of adsorbent, pH, contact time, and initial concentration of fluoride ions) with a face-centered feature (-1, 0, and + 1) as displayed in Table 1. Fluoride adsorption tests were carried out in batch mode utilizing a cellulose/HAp nanocomposite adsorbent. The adsorption experiments were conducted under range value of process variables (dosage (0.75–1.75 g/L), pH (5–9), initial concentration (20–40 mg/L), and contact time (40–80 min)) at a temperature of 30 ± 1 °C. Stock solutions at various specified concentrations were prepared using sodium fluoride (NaF). The adsorption was carried out using 100 mL working solutions in 250 mL conical flasks. Cellulose/HAp nanocomposite adsorbent doses were added to a 100 mL working solution. The contents of the flasks were stirred using a magnetic stirrer at 200 rpm for the necessary duration. The adsorbent was separated by centrifuge at the end of the adsorption process, and the residual fluoride was determined using a fluoride ion-selective electrode (Jenway, model 3345, made in England). The fluoride removal percentage was calculated by Eq. (2), and the adsorption capacity (AC) was calculated using Eq. (3).

Factors	labels		
	Low (-α)	Medium (0)	High (+α)
Adsorbent dose (g/L)	0.75	1.25	1.75
pH	5	7	9
Initial concentration (mg/L)	20	30	40
Contact time (min)	40	60	80

Table 1. Process variables with lower, medium and upper labels.

$$\mathrm{R}\ (\%) = \frac{C_i - C_e}{C_i} * 100 \tag{2}$$

$$AC\ \ (mg/g) = \frac{C_i - C_e}{M} * V \tag{3}$$

where: C_i and C_e were the initial and equilibrium concentrations of fluoride (mg/L) respectively. The M and V were the mass of the adsorbent, and the volume of the working solution, respectively.

According to the CCD design for four factors, the 30 batch experiments were carried out. Among 30 trials, 6 experiments were replications at center points. ANOVA analysis confirmed the investigated variables' hypotheses and tolerability. The response parameter (removal efficiency) was predicted via a polynomial equation under designed condition using Eq. (4)

$$R(\%) = B_o + \sum_{i=1}^{k} B_i X_i + \sum_{i=1}^{k} B_{ii} X_i^2 + \sum_{i>j}^{k} \sum_{j}^{k} B_{ij} X_i X_j + \varepsilon \tag{4}$$

where: R is the response variable; B_o is the intercept at the center; X_i and X_j refer to independent parameters; B_i, B_{ii}, and B_{ij} are regression coefficients; and ε is the error.

Adsorption isotherm

The study evaluated the adsorption isotherms at optimum conditions. The isotherm models: Langmuir, Freundlich and Temkin, and were analyzed to determine the most suitable one for describing or predicting the adsorption of fluoride ions onto cellulose/Hap nanocomposite adsorbent. The Langmuir isotherm was correlated using Eq. (5)

$$\frac{C_e}{q_e} = \frac{1}{q\max * K_L} + \frac{1}{q\max} * C_e \tag{5}$$

where: the equilibrium adsorption capacity is denoted by q_e (mg/g), the maximum adsorption capacity by q_{max} (mg/g), the equilibrium fluoride ion concentration is denoted by C_e (mg/L), and the Langmuir adsorption constant is represented by K_L. Equation (6) was used to get the crucial isolation factor (R_L). Reversibility occurs when R_L=0, linearity occurs when R_L=1, unfavorability occurs when R_L>1, and favorability occurs when $0 < R_L < 1$.

$$R_L = \frac{1}{(1 + K_L C_o)} \tag{6}$$

Freundlich isotherm model was correlated using Eq. (7)

$$q_e = \ln K_F + \frac{1}{n} \ln C_e \tag{7}$$

where: K_F and n are the Frendlich model's isotherm constants.

The Temkin isotherm considers the interaction between adsorbent and adsorbate, based on the concept of the free energy of desorption[22]. The correlation was determined by utilizing Eq. (8).

$$q_e = B_T \ln A_T + B_T \ln C_e \tag{8}$$

where: A_T is equilibrium binding constant and B_T is Temkin isotherm constant.

Adsorption kinetics

Fitting the kinetic model to experimental data is crucial for the design of adsorption processes. The pseudo-second and pseudo-first order kinetic models were verified to select the best one describing the experimental data of fluoride ion adsorption in the tested system. Equation (9) was utilized to determine and relate the pseudo-first-order kinetic model, whereas Eq. (10) was employed to evaluate the pseudo-second-order kinetic model.

$$\ln(q_e - q_t) \ = \ln q_e - K_1 t \tag{9}$$

$$\frac{t}{q_t} = \frac{1}{K_2 {q_e}^2} + \frac{1}{q_e}\ (t) \tag{10}$$

where: t (min) is the contact duration, q_t (mg/g) is the amount of fluoride ion adsorbed at variable time (min), and K_1 (1/min) and K_2 (g/(mg·min)) are the rate constants of pseudo first and second-order adsorption respectively.

Adsorption thermodynamics

In designing the adsorption process, thermodynamic factors expressed as state functions are important, i.e. enthalpy (ΔH), entropy (ΔS), and Gibbs free energy(ΔG°). These values were determined based on studies on the influence of temperature on the adsorption process. Comprehending the thermodynamics of adsorption is essential for identifying the type of process and reaction occurring during the process. Enthalpy quantifies energy trapped in bonds, while entropy represents system changes during adsorption. The adsorption spontaneity is

described by the standard Gibbs free energy change. Equations (11, 12, and 13) were utilized to correlate these parameters.

$$\triangle G^o = RT \ln K_c \tag{11}$$

$$\ln K_c = \frac{\triangle S^o}{R} - \frac{\triangle H^o}{RT} \tag{12}$$

$$\triangle G^o = \triangle H - T \triangle S \tag{13}$$

Where; K_c is the distribution coefficient, T is temperature (°K) and R is gas constant (8.314 J/mol.K). K_c was calculated using Eq. (14).

$$K_c = \frac{q_e}{C_e} \tag{14}$$

Desorption and regeneration of the adsorbent

Desorption of fluoride ions from the adsorbent was conducted after each adsorption experiment. After the adsorption process, the adsorbent was rinsed with distilled water and then dried at 95 °C for one hour, as described in the literature[23]. The sample was stirred with a regeneration solution consisting of NaOH (0.1 mol/L, 100 mL) for 1.5 h. From adsorbent synthesis and application to desorption process was shown in Fig. 1.

Fluoride adsorption mechanism

Fluoride adsorption using a nanocomposite made of cellulose and HAp could occur by physisorption or chemisorption. The primary process was physical adsorption; thus, the addition of cellulose to the composite material increased surface area and porosity, potentially increasing the number of active cites that adsorb fluoride ions through them. Furthermore, proposed adsorption processes included ion exchange and electrostatic interactions. HAp can absorb fluoride ions because it can exchange hydroxide ions and during nanocomposite production, negatively charged cellulose can attract positively charged calcium ions, which can then attract fluoride ions.

Results and discussion

Characterization result of adsorbent materials

Determination of particle size distribution

The particle size distribution obtained for cellulose, HAp, and cellulose/HAp nanocomposite were presented in Fig. 2(a, b, and c) respectively. The results from the analysis from DLS are collected in Table 2. The intensity weighted mean hydrodynamic size of the particles (Z-average in nanometer), Poly-Dispersity Index (PDI), and materials quality are critical parameters to examine the DLS result[24,25].

The Z-average sizes of cellulose, HAp, and cellulose/ HAp nanocomposite were 54.49 nm, 79.70 nm, and 78.93 nm, respectively. These average sizes were less than 100 nm, suggesting all these samples are in the nanomaterial category. The PDI score of 0 implies that the sample particles are perfectly uniform, whereas 1

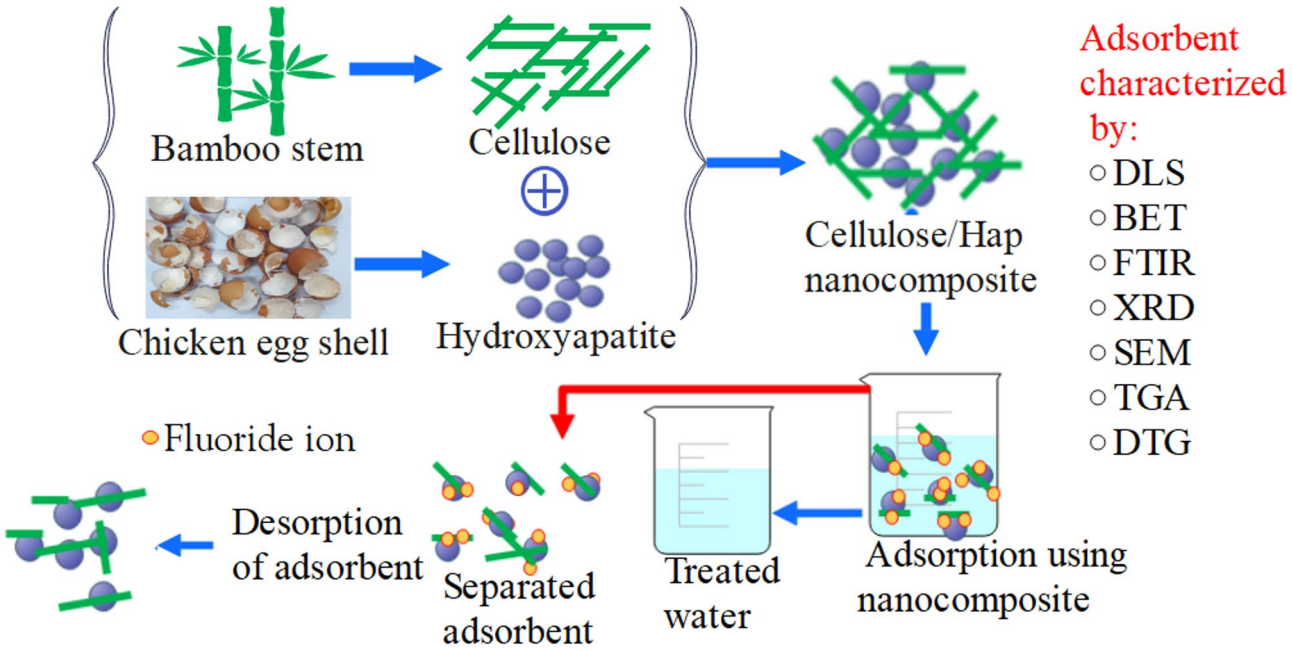

Fig. 1. Schematic representation of adsorbent synthesis, characterization adsorption and desorption.

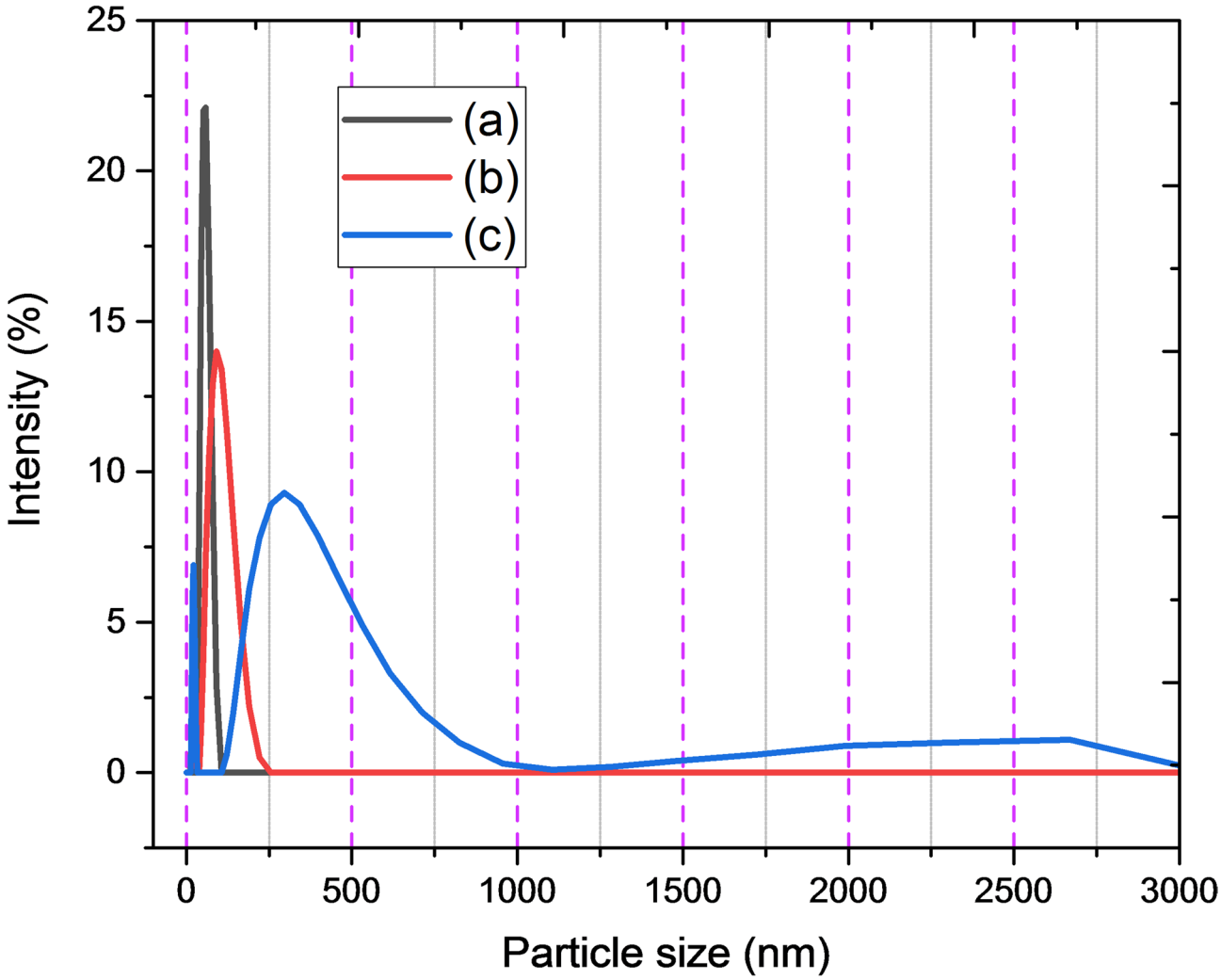

Fig. 2. Size distribution of cellulose (**a**), HAp (**b**) and cellulose/HAp nanocomposite (**c**).

Samples	Z-Average (d.nm)	PDI	Result quality
Cellulose	54.49	0.10	Good
HAp	79.70	0.29	Good
Cellulose/ HAp nanocomposite	78.93	1.00	Good

Table 2. The particles size distribution information obtained from DLS result.

shows a high level of polydispersity in the sample (many peaks)[26]. The PDI of cellulose was 0.10, demonstrating the homogeneity of the sample, as seen in Table 2. The PDI of HAp was 0.29, whereas the PDI of cellulose/HAp nanocomposite was 1.0. These PDI values suggest that HAp is polydisperse, whereas cellulose/HAp is highly polydisperse. The non-uniform distribution of particle sizes in the cellulose/ HAp nanocomposite suggests that agglomeration occurred during the incorporation of cellulose and HAp, which conformed to the nanocomposite formation. There are no smallest-sized particles present in the cellulose/HAp nanocomposite compared to the individual particle sizes of HAp and cellulose. The second minor peak in the cellulose/HAp nanocomposite indicates the presence of particles measuring 21.09 nm, which are larger than the smaller particles in HAp (20.22 nm). The correlation finding suggests that nanocomposite was effectively synthesized using cellulose and HAp.

Textural properties analysis

The textural characteristics of cellulose, HAp, and cellulose/HAp nanocomposite were determined by BET analysis. The results obtained are shown in Table 3. The average pore diameters of cellulose, HAp, and cellulose/HAp nanocomposite before and after adsorption were 10.87 nm, 15.25 nm, 18.93 nm, and 7.82 nm, respectively.

The pore diameter of the cellulose/HAp nanocomposite was highest before adsorption. This was due to the negatively charged hydroxyl group being substituted with positively charged calcium ions, leading to an increase in pore size. The BET analysis results were well correlated with the SEM analysis results displayed in Fig. 3. The specific surface area of the cellulose/HAp nanocomposite decreased from 223.67 to 141.21m^2/g after adsorption. This reduction was caused by the filling of porous media with adsorbate material and the leaching of active sites into the reaction media. The specific surface area cellulose/HAp nanocomposite before adsorption shown in Table 3 was highest when compared with other adsorbents' specific surface area, such as hydroxyapatite/ nanotubes (178.65 m^2/g)[27]Hydroxyapatite nanorods (21.25 m^2/g)[28] and cellulose- layered nanocomposite (1.21) m^2/g[29]. The specific surface area rose concurrently with the pore volume of the adsorbent materials. In this work, the specific surface area of cellulose, Hap, and the cellulose/Hap nanocomposite rose in a manner consistent with the rise in pore volume. This confirmed with literature[30]. The pore type of these adsorbent materials is mesoporous, which is in between 2 and 50 nm[30,31].

The increment of specific surface area in cellulose/HAp nanocomposite adsorbent that was used in the current experiment was due to the substitution of negatively charged ions with positively charged calcium ions that come from HAp.

SEM results

The SEM was used to analyze the surface morphology of cellulose, HAp, and cellulose/HAp nanocomposite before and after adsorption. Figure 3 displays the resulting images at various resolutions (a, b, c, d). Analyzing SEM pictures of cellulose (Fig. 3(a)), the interconnected fibers network of cellulose is observed. Furthermore, irregular and tiny pores are visible. The structure of the produced cellulose confirms, that the applied procedure of bamboo extraction was effective under the recommended optimal conditions outlined in the literature by treating it with a combination of two acids[17]. Figure 3(b) displays SEM images at different resolutions showing the surface characteristics of the synthesized HAp. The SEM image revealed several clustered bundles of nano-rod-like structures aligned with other findings[28,29]. To improve surface characteristics (increase specific surface area, porosity and enhance morphology) of the adsorbent, HAp should be modified by incorporating cross-linking ingredient.

Figure 3(c) shows a complete lamellar structure in the cellulose/HAp nanocomposite adsorbent. Additionally, a heterogeneous layer established a network that linked the particles. This suggests that cellulose layers are bonded with HAp particles, leading to the formation of a composite. The sample's high porosity is due to proper preparation and the HAp particles binding to the cellulose surface. The specific surface area increases resulted from pore formation in the cellulose/HAp nanocomposite adsorbent that was correlated with the BET results. This enhances the adsorbent's capacity and facilitates the diffusion of adsorbed ions. Figure 3(d) displays a surface morphology of the cellulose/HAp nanocomposite adsorbent after use. SEM image reveals the formation of agglomerates and a reduction in pore size. This occurred due to the adsorbate filling the porous medium and the leaching of active sites into the reaction medium.

FTIR analysis

The cellulose, HAp, cellulose/HAp nanocomposite's significant functional groups were analyzed using FTIR analysis before and after adsorption, with the findings shown in Fig. 4. The faint and wide signal between 3300 and 3400 cm^{-1} in cellulose and HAp corresponds to the O-H functional group[28]. The weak peak indicates that the materials were thoroughly dried and lacked sufficient moisture content in the samples. The spectra of the cellulose/ HAp nanocomposite showed a wider peak before and after usage compared to the peaks observed in cellulose and HAp individually. The nanocomposite's larger moisture content was linked to the O-H stretching bond. The peak at 2900 cm^{-1} in cellulose and nanocomposite is attributed to C-H, -CH_2, and -CH_3 vibrations from alkyl groups. Additionally, a peak related to C=O stretching is seen at 2164 cm^{-1}[32]. HAp lacks peaks associated with alkyl and carbonyl groups. The prominent peak at 1630 cm^{-1} corresponds to the NH_4^+ bending vibration mode in both the cellulose/HAp nanocomposite samples before and after adsorption. The NH_4^+ from urea is used in the production of the nanocomposite[28]. The peak at 1458 cm^{-1} is caused by the vibrational mode of CO_3^{2-} in the carbonated material[21]. The prominent peak at 1030 cm-1 is associated with the bending vibrations of PO_4^{3-} in HAp, cellulose/HAp nanocomposite, both before and after the adsorption of substances in HAp [27]. The cellulose sample has a peak at 1030 cm^{-1}, indicating a mild stretching vibration of C-O groups[33]. The peak at 558 cm^{-1} in the HAp, cellulose/HAp samples before and after adsorption is linked to the P-O-P vibration mode. The lack of this distinctive peak in the cellulose sample suggests the absence of P-O-P groups in cellulose[34].

Samples	Pore size (nm)	Specific surface area (m^2/g)	Pore volume (cm^3/g)
Cellulose	10.87	78.33	0.71
HAp	15.25	169.43	0.74
Cellulose/HAp nanocomposite	18.93	223.67	1.17
Cellulose/HAp nanocomposite after adsorption	7.82	141.21	0.63

Table 3. Textural properties of adsorbent materials in current study.

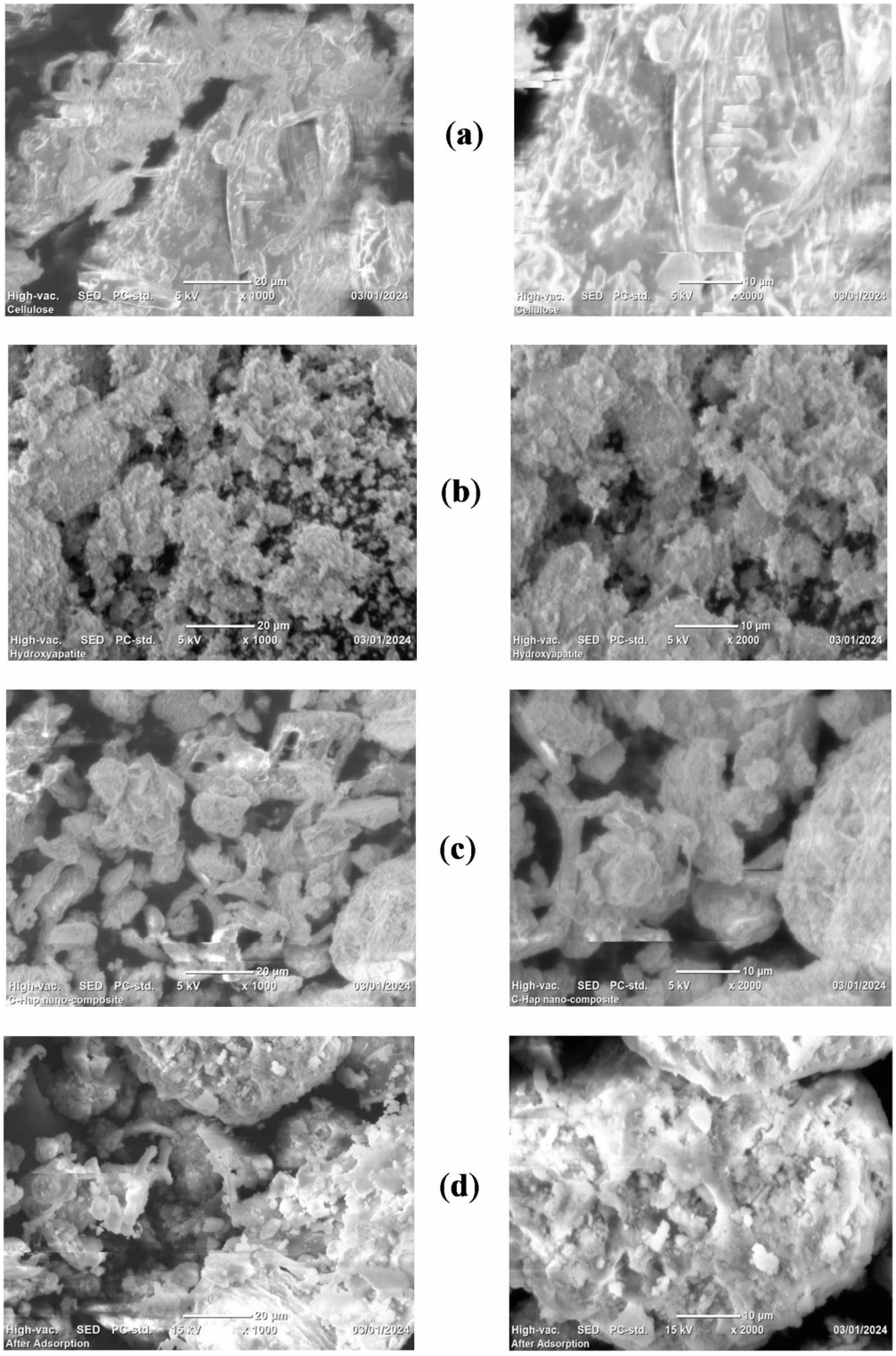

Fig. 3. SEM images of cellulose (**a**), HAp (**b**), cellulose/ HAp nanocomposite before adsorption (**c**), and cellulose/Hap nanocomposite after adsorption (**d**).

XRD analysis

The X-ray diffraction patterns of cellulose, HAp, and a cellulose/ HAp nanocomposite were analyzed. Figure 5(a) shows the XRD pattern of cellulose with peaks at $2\theta = 22.62$, 29.34, 44.31, 64.34, and 77.47°, which represent 19.21, 1.60, 0.77, 0.50, and 0.88% of the crystalline index respectively. Figure 5(b) displayed distinct peaks associated with HAp. These peaks at $2\theta = 22.62$, 29.34, 31.62, 35.71, 39.32, 43.98, 47.29, and 48.28° correspond to crystalline indexes of 1.39, 13.52, 6.13, 1.92, 2.26, 1.77, 3.15, and 2.96%. The XRD pattern of HAp synthesized in

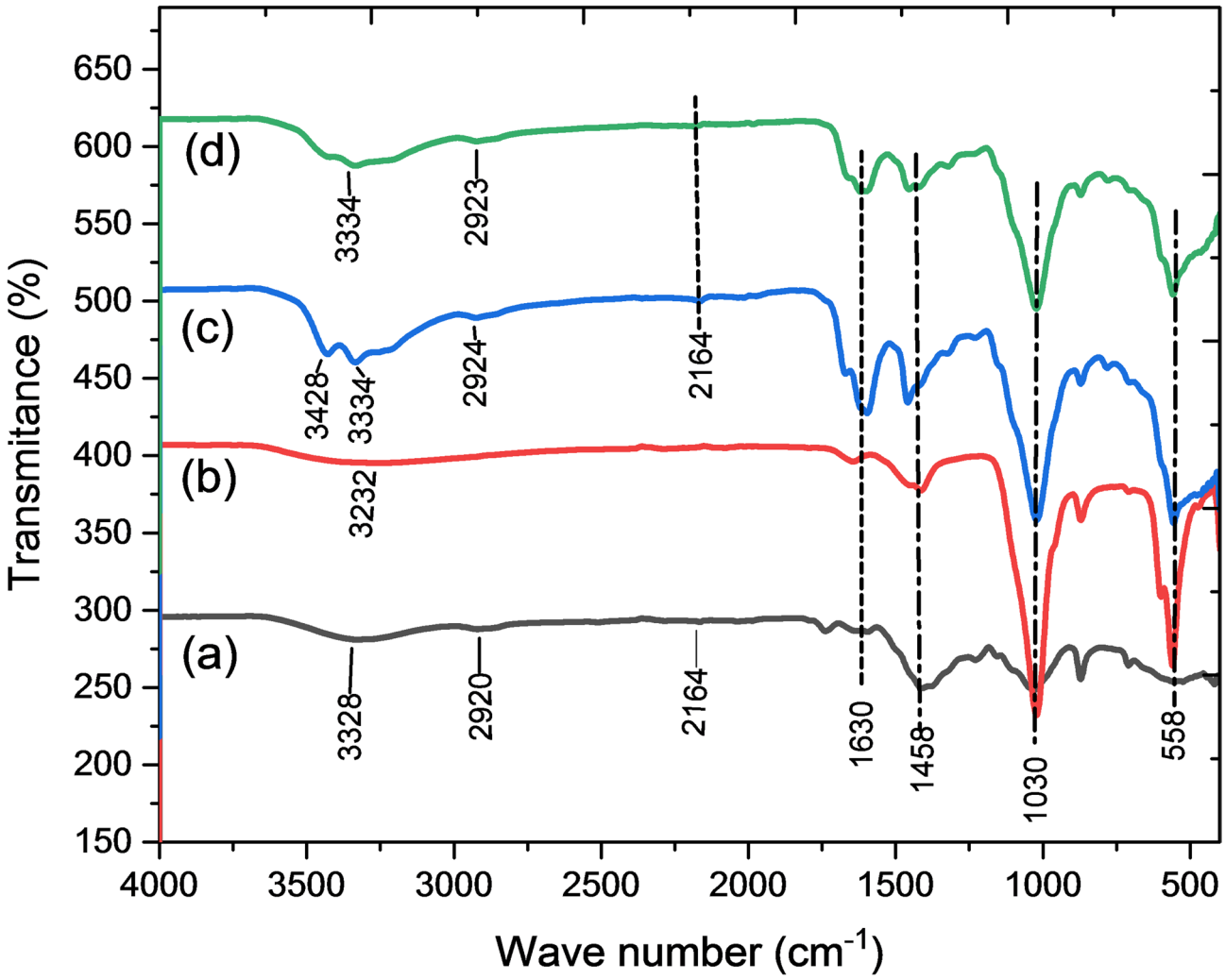

Fig. 4. FTIR result of cellulose (**a**), HAp (**b**), and cellulose/HAp nanocomposite before adsorption (**c**) and cellulose/ HAp nanocomposite after adsorption (**d**).

the current work matched the XRD pattern of HAp in the literatures[20,34]. Figure 5(c) displays peaks at 2θ = 22.62, 29.34, 31.62, 35.71, 39.32, 43.98, 47.29, 48.28°, indicating the crystalline index of 5.12, 5.96, 4.21, 1.61, 2.23, 1.4, and 2.46% in the cellulose/HAp nanocomposite. The crystalline index (5.12%) at 2θ = 22.62° in the cellulose/ HAp nanocomposite is in the range of the crystalline index of cellulose (19.21%) and HAp (1.39%), indicating an intermediate outcome. Similarly, the peak at 2θ = 29.34° indicates the crystalline index in cellulose (1.60%), HAp (13.52%), and cellulose/ HAp nanocomposite (5.96%). This suggests that the overlapping peaks led to an intermediate crystalline index in the nanocomposite. The findings of the crystalline index at these two peaks confirmed the formation of a nanocomposite from cellulose and HAp.

Thermal properties

The thermal characteristics of cellulose, HAp, and cellulose/HAp nanocomposite were studied using thermogravimetric (TGA) and derivative thermogravimetric (DTG) analysis. Each material had varying thermal stability at different degradation temperatures. Figure 6 shows that the cellulose sample degraded more quickly than the HAp and nanocomposite samples. Cellulose samples lost 5.22% of their weight up to 105 °C, whereas HAp and nanocomposite lost 1.53%. Cellulose's hydrophilic nature allows it to absorb moisture. The evaporation of volatile substances, moisture content, and physically adsorbed compounds caused slight weight reductions in all samples[32].

The DTG graph in Fig. 7 indicates that the cellulose sample reached a maximum temperature of 441.02 °C during weight loss. Cellulose loses around 81.23% of its weight at this temperature. This was due to the degradation of hemicellulose and cellulose structures[35]. At 441.02 °C, the nanocomposite saw a weight loss of approximately 41.92%, whereas HAp lost around 6.08%. HAp exhibited greater stability compared to the cellulose and nanocomposite samples, aligning with findings from a prior study[19]. The study found that adding cellulose to hydroxyapatite particles helps the thermal stability of the nanocomposite. This occurred robust interaction between cellulose and HAp particles. The HAp exhibited heat stability up to 700 °C. At temperatures

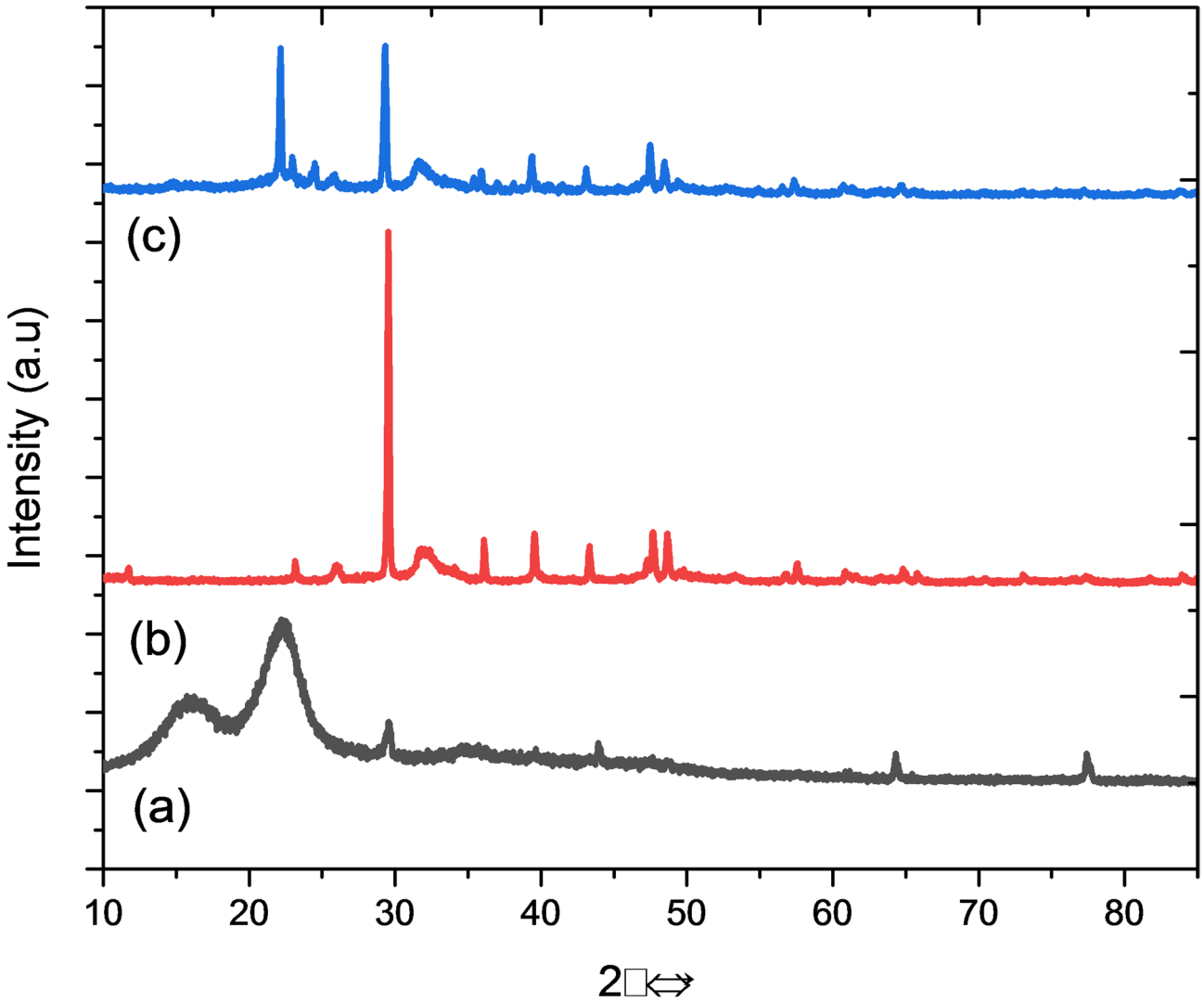

Fig. 5. XRD diffraction of cellulose (**a**), HAp (**b**), and cellulose/HAp nanocomposite (**c**).

above 700 °C, HAp began to show thermal deterioration. It is caused by the bond disruption inside and between molecules at elevated temperatures[36]. The DTG graph in Fig. 7 shows cellulose losing around 81.23% of its weight at this temperature. The nanocomposite experienced approximately 30% weight loss at its maximum degradation temperature of 321 °C. The study found that the synthesized nanocomposite had high thermal stability, making it appropriate for adsorbing fluoride from water at low temperatures.

Experimental results and statistical analysis

Table 4 shows the experimental design matrix and the accompanying response data. The experimental results for defluoridation efficiency were examined using the CCD plan of the experiment. Sorbent dosage, contact duration, pH, and initial concentration of fluoride ions labeled by codes A, B, C, and D were selected as crucial factors in the adsorption experiments. A quadratic model was proposed to forecast the response variable within a specified range of values. ANOVA confirmed the model's appropriateness. The experiments' reliability was assessed based on lack of fit, P-value, F-value, and precision adequacy. Key factors for model validity assessment are collected in Table 5. According to ANOVA theory coefficient terms with a P-value below 0.01 are considered significant, whereas those above are not. The high F-value, and low P-value (<0.0001) are characteristic of the significant model. F and P values are key parameters in model-experimental result interpretation[37,38]. Large F-vale and small P value suggests that the design experiment was well fitted with experimental variations that confirm the quadratic model[39]. The ANOVA analysis indicated that linear terms (A, B, C, and D), quadratic terms (A^2 and C^2, and interaction terms (AB, AC, AD, and CD) were statistically significant[40]. The increase in parameters represented by A and C reflects their positive impact on the removal effectiveness of fluoride ions with the cellulose/HAp nanocomposite adsorbent. An increase in A enhances the surface area available for fluoride ion adsorption, whereas an increase in B prolongs the contact time between the adsorbent and adsorbate. An optimal value of B resulted in the highest removal efficiency, whereas an increase in D resulted in a reduction in removal efficiency. The dependability of experimental findings was confirmed by the higher

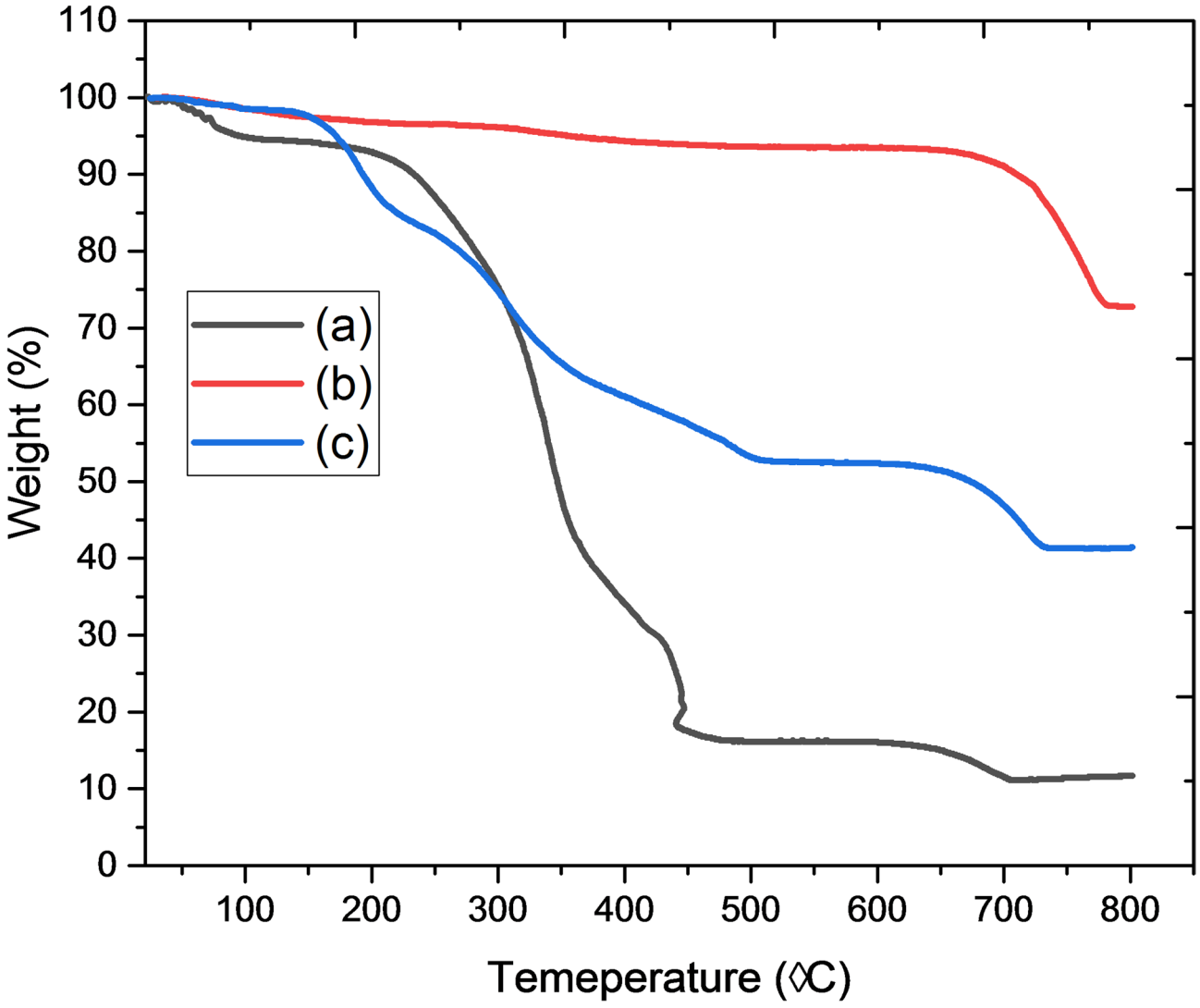

Fig. 6. TGA profile of cellulose (**a**), Hap (**b**) and cellulose/Hap nanocomposite (**c**).

coefficient of variation terms ($R^2 = 0.991$, adjusted $R^2 = 0.982$, projected $R^2 = 0.958$) displayed in Table 5. The proximity of coefficient terms suggests that the observed response levels closely align with the expected values. The coefficient of variance in Table 5 shows that the data is highly repeatable. The actual removal efficiency compared to predicted values, residual plots and box-cox plot, respectively was presented in Fig. 8 (a, b, c). It can be seen the actual and predicted response levels were closely aligned. This was confirmed by the even distribution of residuals on the normal plot (Fig. 8b). The experimental results were mostly consistent with the prediction model[41].

Figure 8(a, b, c) The actual versus predicted removal efficiency, normal plot of residuals, and Box-Cox plot for transforms. The actual and pridcted removal efficiencies distributed uniformly on linear line and also the residual was evenly distributed. In addition, A logarithmic transformation is the most successful method, according to the Box-Cox plot, which shows that the ideal transformation for the data is $\lambda = 0$. In order to improve the model's fit, a log transformation can assist stabilize the variance and make the data more regularly distributed. As a result, using the log transformation ought to improve the analysis and prepare the data for statistical techniques like regression[39]. The developed model can be applied to predict the response value within the specified range of process variables. The equation was constructed by identifying the central point of the design space of process variables. The alteration in removal efficiency, R (%) of cellulose/HAp nanocomposite can be correlated using Eq. (15) by removing non-significant terms (interaction terms: BC and BD, and quadratic terms: B^2 and D^2 of coded variables.

$$R(\%) = 92.57 + 6.48 * A - 2.95 * B + 6.08 * C - 5.58 * D + 1.30 * A * B - 2.36 * A * C - 1.71 * A * D + 1.84 * C * D - 5.43^{*}A^2 - 3.64^{*}C^2 \quad (15)$$

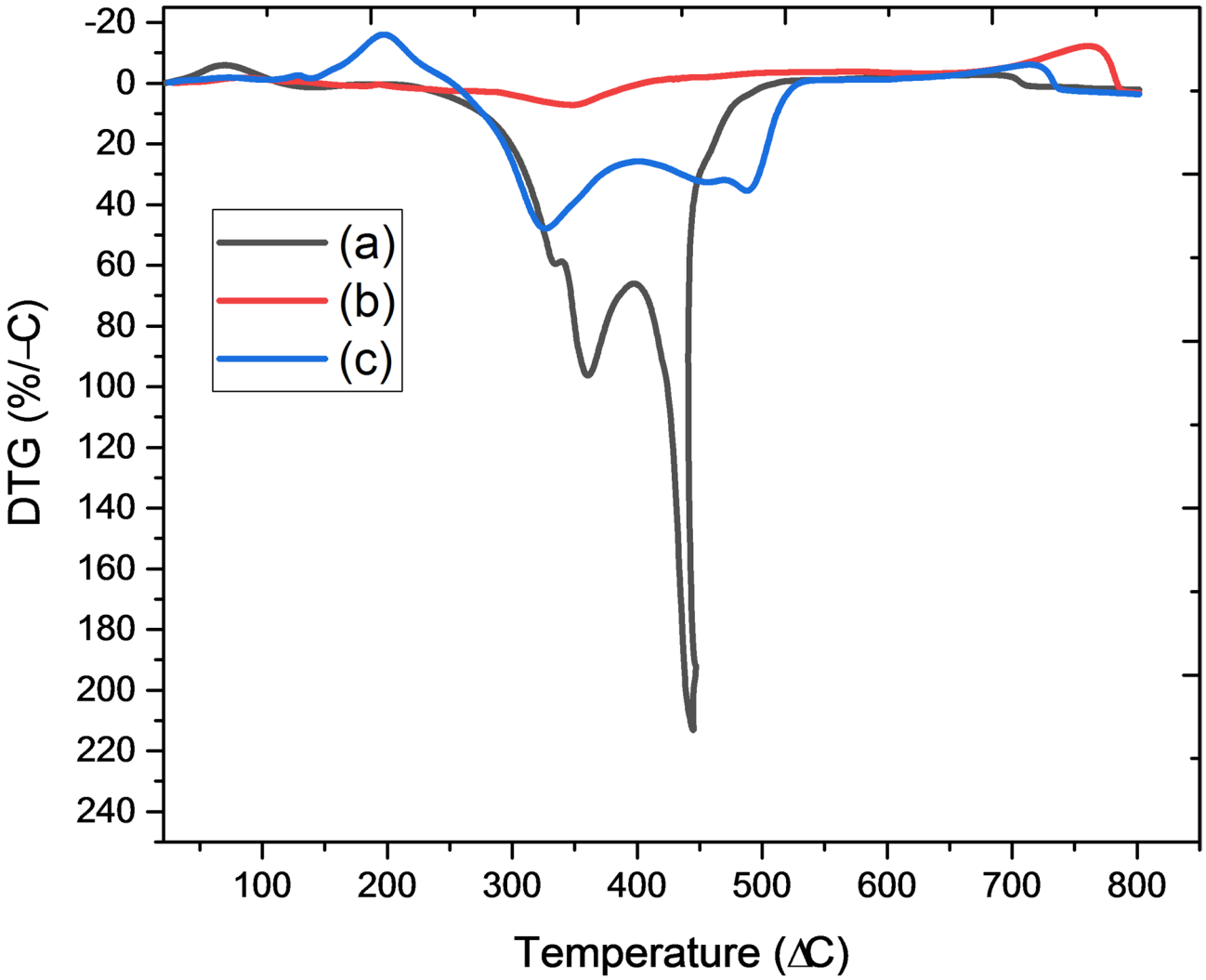

Fig. 7. DTG curves of cellulose (**a**), HAp (**b**) and cellulose/ HAp nanocomposite (**c**).

Combined effect of process variable

Interaction effect of pH and dose

Figure 9(a) illustrates the combined impact of adsorbent dosage and pH in a 3D surface plot. Increasing the dose from 0.75 to 1.75 while maintaining pH, initial concentration, and contact duration at medium levels improved the removal efficiency from 78.58 to 95.18%. This was because more active sites were available at greater dosages. As the pH increased from 5 to 7, the removal efficiency decreased from 96.06 to 85.37%. However, a further increase in pH, in the range of 7 to 9, resulted in a significant decrease in the efficiency of fluoride ion removal. This might be attributed to the generation of hydroxide ions on the surface of the cellulose/HAp nanocomposite adsorbent. An increase in the adsorbent dose was shown to enhance the elimination efficiency at lower pH levels. This result was consistent with previous defluoridation experiments that were reported[42].

Interaction effect of contact time and dose

The effects of the adsorbent dosage and contact time on the removal of fluoride ions are shown in Fig. 9(b) as a 3D surface plot. Defluoridation rose when both factors increased. A removal efficiency of 98.31% was achieved with a dose of 1.75 g/L, a contact time of 80 min when an initial fluoride concentration was 20 mg/L, and a pH of 5. This is resulted from increase of duration of adsorption of adsorbate on the surface of adsorbent and increase of adsorbent amount results in adsorption of more adsorbate material, which enhances the removal efficiency[43]. Elevating these variables above the limit may cause a minor reduction in fluoride removal performance, as shown in Fig. 9(b). Over an extended period, the driving force for mass transfer between the solid and liquid phases may diminish[23]. This finding was consistent with the defluoridation experiments described earlier[42].

Interaction effect of dosage and initial F^- concentration

Figure 9(c) shows the 3D surface plot presenting the influence of adsorbent dose and initial fluoride concentration on the removal efficiency. Increasing the adsorbent amount improved removal efficiency, however, increasing the initial fluoride concentration decreased it. The considerable impact of process variables interacting with each

Run	Dosage (g/L)	pH	Contact time (min)	Initial concentration (mg/L)	Actual removal efficiency (%)	Predicted removal efficiency (%)
1	1.25	7	60	40	85.16	85.92
2	1.25	7	80	30	95.37	95.01
3	1.25	9	60	30	85.37	88.02
4	1.25	7	60	20	97.29	97.03
5	1.25	5	60	30	96.06	93.92
6	1.25	7	40	30	81.97	82.84
7	0.75	9	40	20	68.86	68.38
8	0.75	5	40	40	63.74	64.15
9	0.75	5	40	20	75.47	74.76
10	0.75	5	80	40	86.84	86.07
11	0.75	5	80	20	88.09	89.32
12	0.75	9	80	40	75.84	75.47
13	0.75	9	40	40	56.81	56.25
14	0.75	9	80	20	81.07	80.24
15	1.25	7	60	30	93.03	92.57
16	1.25	7	60	30	92.06	92.57
17	1.25	7	60	30	91.87	92.57
18	1.25	7	60	30	92.67	92.57
19	1.25	7	60	30	94.01	92.57
20	1.25	7	60	30	93.27	92.57
21	1.75	7	60	30	95.18	93.61
22	1.75	5	40	40	75.49	75.82
23	1.75	5	80	20	98.31	98.37
24	1.75	5	40	20	92.52	93.26
25	1.75	9	40	20	91.81	92.08
26	1.75	9	80	40	82.66	82.87
27	1.75	9	80	20	94.52	94.49
28	1.75	9	40	40	73.96	73.1
29	1.75	5	80	40	87.44	88.29
30	0.75	7	60	30	78.58	80.66

Table 4. Experimental design matrix, and actual and predicted response values.

Parameters	Results for reliability evaluation
Quadratic model	Significant
Lack of fit	Non-significant
R^2	0.991
Adjusted R^2	0.982
Predicted R^2	0.958
Adequate precision	42.23
Coefficient of variation	1.65%

Table 5. Model adequacy evaluation matrix.

other was demonstrated. The highest fluoride removal rate of 98.31% was attained with an adsorbent dosage of 1.75 g/L and an initial fluoride concentration of 20 mg/L.

Interaction effect of contact time and initial F^- concentration

Figure 9(d) shows the impact of contact time and initial F^- concentration on the removal efficiency of fluoride ions. As these two process variables increased, the defluoridation efficiency decreased. The fluoride removal efficiency was 97.29% at an initial concentration of 20 mg/L and 85.16% at 40 mg/L, using a dose of 1.25 g/L and a pH of 7. At 40 min and 80 min, with all other parameters held constant at a moderate level, the removal efficiency was 81.97% and 95.37%, respectively. Extended contact time increased the efficacy of fluoride removal, aligning with an earlier study[44]. Conversely, higher starting concentrations caused decreased defluoridation, similar to other studies[45]. Increasing the contact time between the adsorbate and adsorbent surface resulted

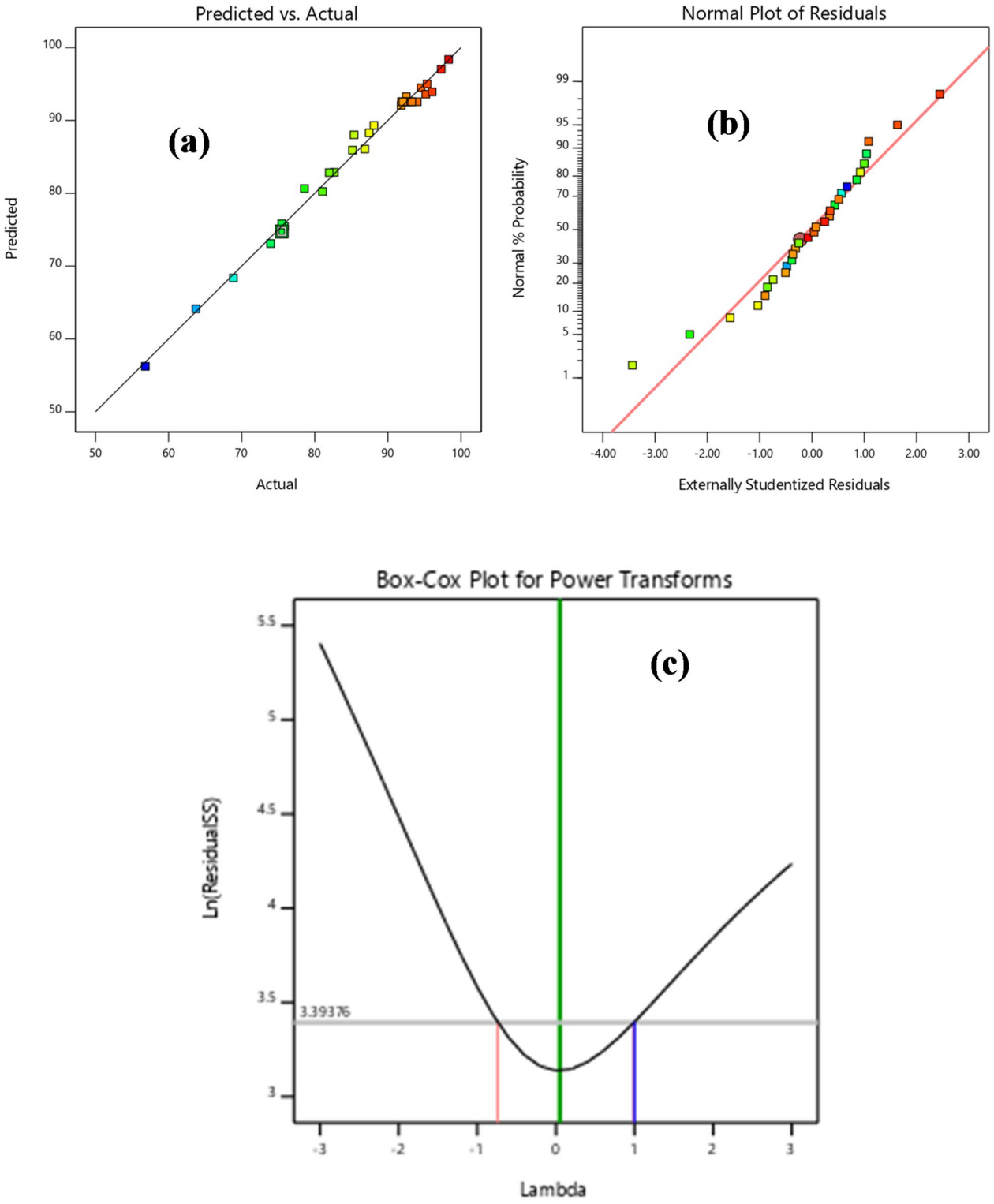

Fig. 8. The actual versus predicted removal efficiency (**a**), normal plot of residuals (**b**), and Box-Cox plot for transforms (**c**).

in higher removal efficiency. Furthermore, the increase in the initial concentration surpassed the number of available active sites in the adsorbent.

Optimization of process condition and validation of the optimized condition

Optimization was conducted using Response Surface Methodology (RSM) in Design Expert software. The objective was to optimize fluoride removal efficiency (the response variable). Four key process parameters: dosage

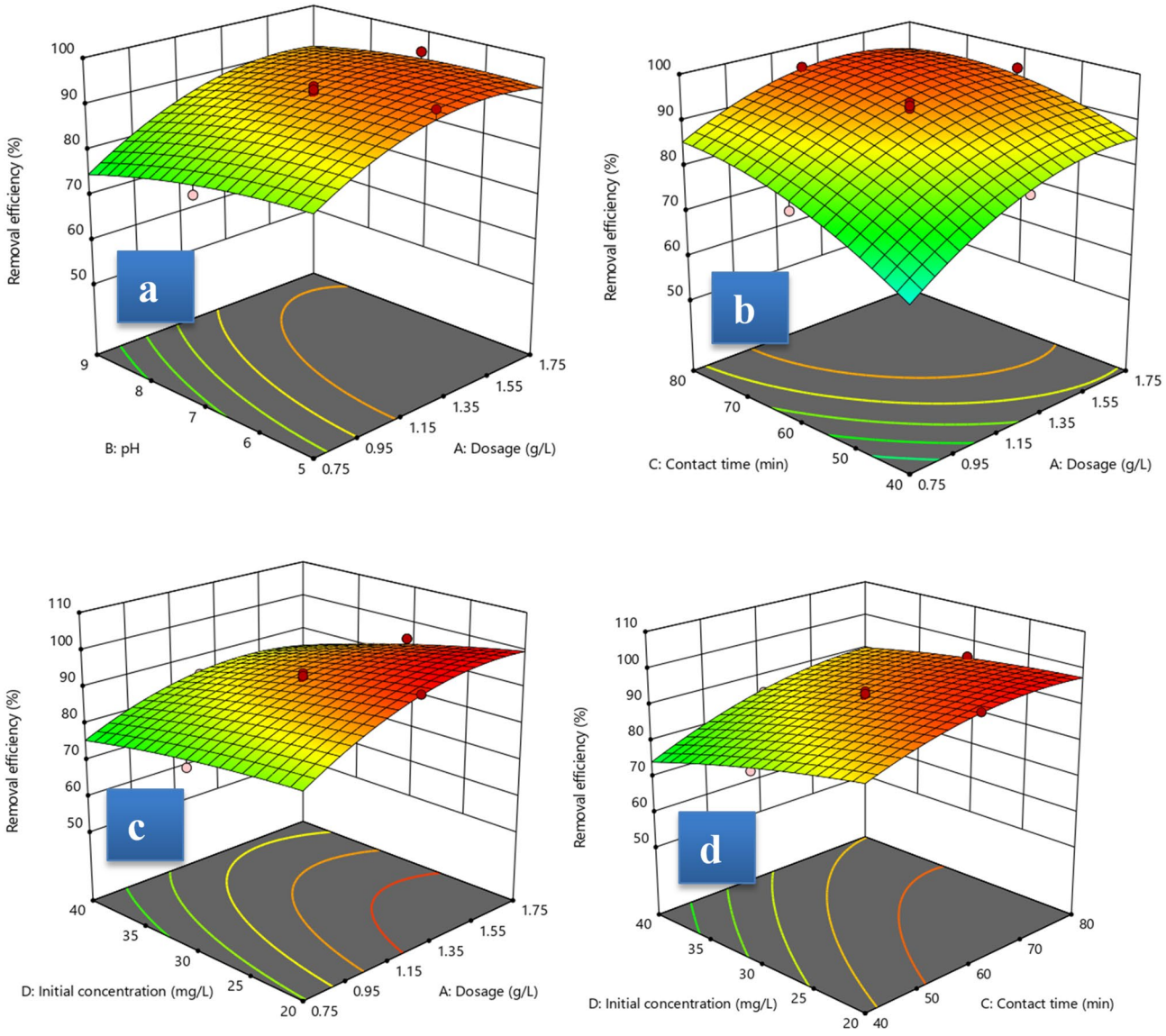

Fig. 9. 3D plots of the interaction effect of investigated variables on defluoridation experiment.

Process variables	Unit	Optimum results
Adsorbent dose	g/L	1.43
pH		5.24
Contact time	min.	77
Initial concentration	mg/L	24.43
Removal efficiency from software	%	99.50
Removal efficiency from the experiment Difference in average of triplicate and predicted	% %	98.68 0.82
Standard deviation of triplicates		0.71
Desirability	--	1

Table 6. Optimum conditions and result validation.

of sorbent, pH, contact time, and initial fluoride concentration were examined, within a specific range given in Table 1. Obtained results are shown in Table 6. The minimal discrepancy of 0.82% between the experimental and predicted value findings indicates that the model fits well with the experimental data. In addition, the highest composite desirability confirms the optimum values. The standard deviation in the triplicate experiment was equal to 0.71. This low value proves the obtained results were not influenced by external interferences. The

optimal conditions for the adsorption of fluoride ions on the obtained cellulose/Hap composite adsorbent are a sorbent dosage of 1,43 g/L, contact time of 77 min, pH of 5,24, and an initial concentration of fluoride of 24.43 mg/L and allowed to reach the highest removal efficiency of 98.68%. These results confirm the high effectiveness of the produced adsorbent in removing fluoride ions.

The high effectiveness of removing F- ions from aqueous solutions using other adsorbents described in the literature, concerned higher doses of the adsorbent, lower F- concentrations in the initial solutions, and longer contact time. The optimal conditions for defluoridation employing Catla (*Catla Catla*) as a bio-adsorbent was a dose of 22.6 g/L, a pH of 9.93, a contact time of 179.49 min, and an initial fluoride concentration of 8.49 mg/L when a maximum fluoride removal of 98.9% was achieved[46]. Another study utilized an activated carbon/aluminum oxide composite as an adsorbent and the removal efficiency was 98% under conditions: a 2.0 g/L dose, a pH of 5.9, 120 min of contact time, and an initial concentration fluoride concentration of 6.0 mg/L[47]. Comparing other adsorbents with our new composite material, it can be concluded that it is a promising sorbent for purifying water from fluoride ions under reasonable optimum conditions.

Adsorption isotherm

The equilibrium isotherm was determined by experiments on the adsorption of fluoride ions from an aqueous solution onto a synthesized cellulose/Hap nanocomposite at pH 5.24 and 30 °C. Under these conditions, the adsorbent had the maximum affinity for fluoride ion adsorption. Fluoride removal adsorption isotherms were analyzed using linear and nonlinear Langmuir, Freundlich, and Temkin models. The initial concentration of fluoride was changed during the assessment of the isotherm models. Figure 10 displayed the graph of the Langmuir isotherm data and Fig. 11 presented Freundlich and Temkin, isotherm models. Figure 12 presents the non-linear plots of these three isotherms in a single graph. The coefficients of determination (R^2 for the linear Langmuir, Freundlich, and Temkin isotherm models were 0.997, 0.963, and 0.964, respectively as shown in

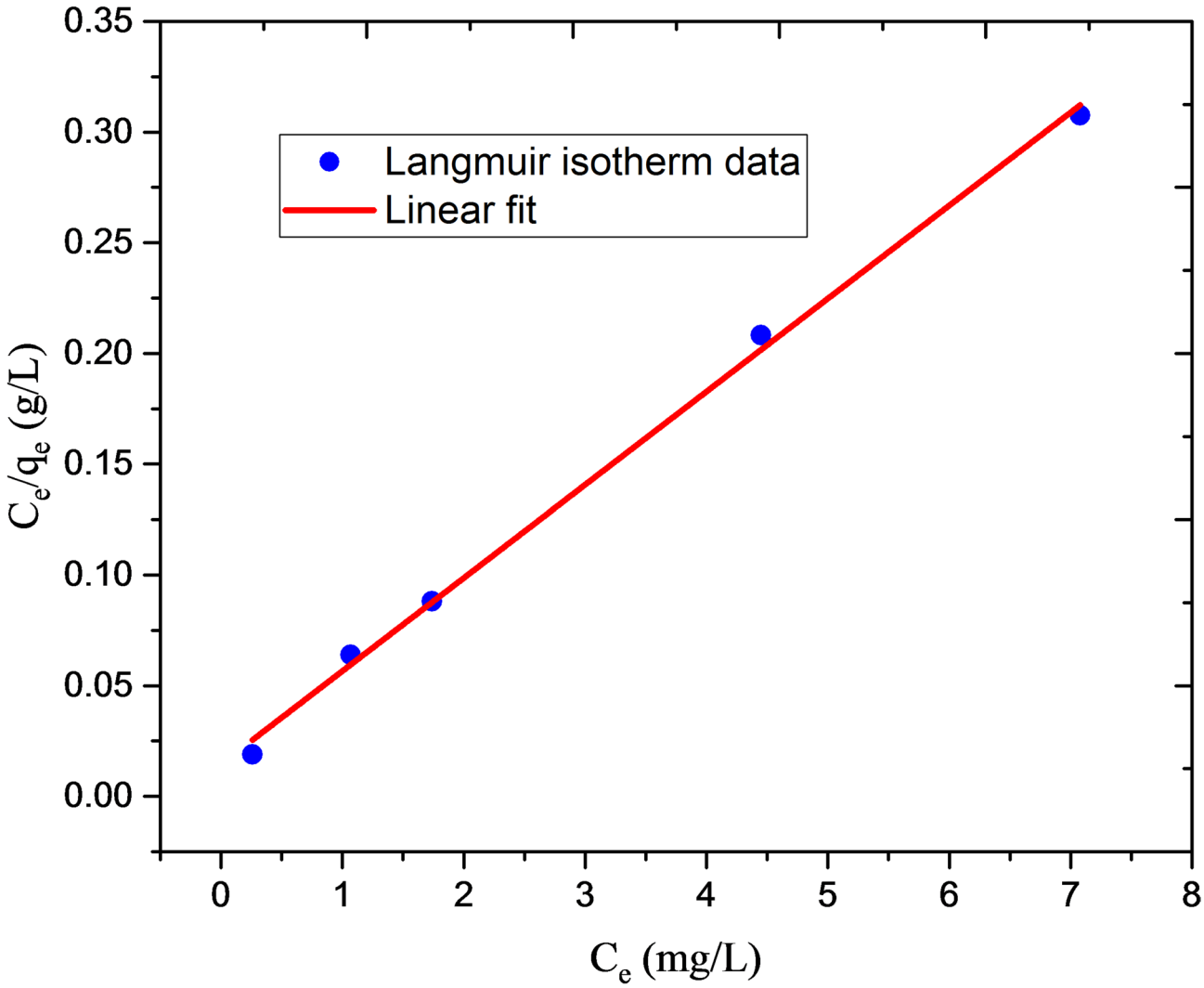

Fig. 10. Plot of Langmuir adsorption isotherm.

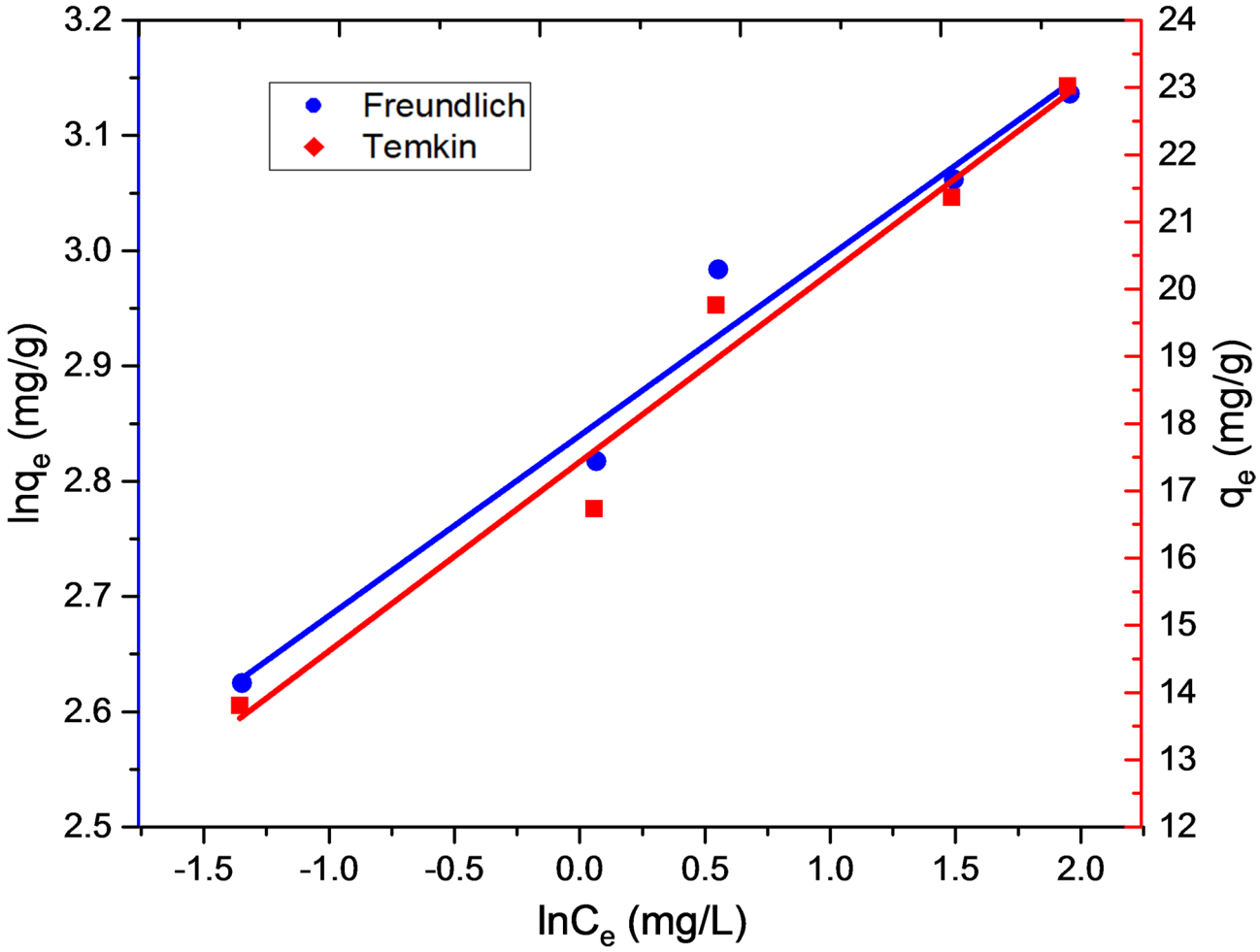

Fig. 11. Plot of Freundlich and Temkin adsorption isotherms.

Table 7. The R^2 values for the non-linear Langmuir, Freundlich, and Temkin isotherm models were 0.947, 0.960, and 0.995, respectively.

The most suitable isotherm model is determined by the one with a higher R^2 value[48,49]. The linear version of Langmuir isotherm can accurately describe the fluoride adsorption for water treatment using cellulose/Hap nanocomposite, as indicated by the determination coefficient. The dimensionless separation factor (R_L) value of 0.014 falls between 0 and 1, suggesting that the adsorption process is favorable[50]. The Langmuir adsorption isotherm is suitable for describing the investigated adsorption process. The experiment shows that the synthesized cellulose/Hap nanocomposite adsorbent is efficient for fluoride adsorption, with a maximum adsorption capacity (q_m) of 23.79 mg/g.

Adsorption kinetics

Studying the kinetic parameters using pseudo-first-order and pseudo-second-order studies can assist in determining the rate of adsorption and provide comprehensive information for describing the adsorption process[43]. Table 8 shows the crucial constraint parameter values for adsorption kinetics models. The pseudo-first-order kinetics by plotting time vs. ln(qt) and pseudo-second-order kinetics by time vs. t/q_t are shown in Fig. 13. Collected in Table 8, the R^2 values for the first and second-order kinetic models are 0.909 and 0.998, respectively. It can be observed that the R^2 value of the second-order kinetic model is greater than that of the first-order kinetics model. In addition, the findings of previous research suggest that this model is the one that most frequently describes the experimental data for F^- adsorption processes[54–56]. A second-order kinetic model is used to describe the process of fluoride ions being removed from the cellulose/Hap nanocomposite by the process of sorption onto the surface[56].

[57]. Also, fluoride adsorption from drinking water using reduced graphene oxide and cuprous oxide was described by the second-order kinetic model[44]. Based on the published data, second-order kinetics is the most suitable representation of the fluoride adsorption process[58].

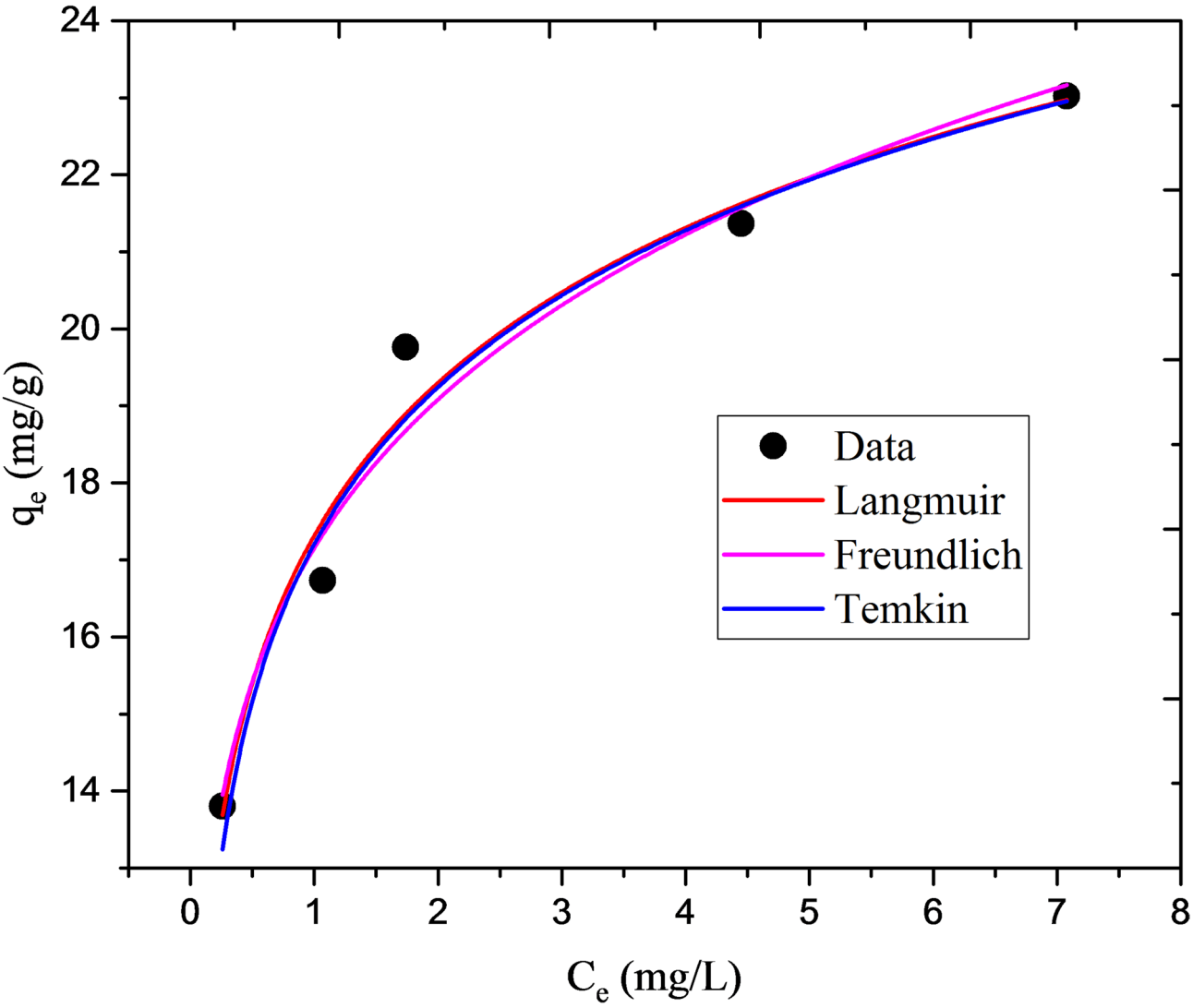

Fig. 12. Graphical representation of non-linear Langmuir, Temkin and Freundlich adsorption isotherms.

Isotherm models	Parameters	Linear isotherm values
Langmuir isotherm model	q_m (mg/g)	23.79
	K_L(L/mg)	2.88
	R^2	0.997
	R_L	0.014
Freundlich isotherm model	n	6.40
	K_F ((mg/g).(L/mg)^1/n)	17.11
	R^2	0.963
Temkin isotherm model	B_T(mg/g)	2.81
	A_T(L/g)	488.39
	R^2	0.964

Table 7. Adsorption isotherm results.

Adsorption thermodynamics studies

Adsorption thermodynamics aims to provide criteria for determining the spontaneity of a process[59]. Thermodynamic characteristics such as changes in enthalpy (ΔH°), changes in Gibbs free energy (ΔG°), and changes in entropy (ΔS°) were determined at various temperatures in the present study. The obtained results are in Table 9. Figure 14 displays the plot of $\ln K_c$ against 1/T for further understanding. The entropy change

Kinetics models	Parameters	Values
Pseudo first order	Q_t (mg/g)	34.284
	K_1(L/mg)	0.077
	R^2	0.904
Pseudo second order	Q_t (mg/g)	18.615
	K_2	0.005
	R^2	0.998

Table 8. Adsorption kinetic models results.

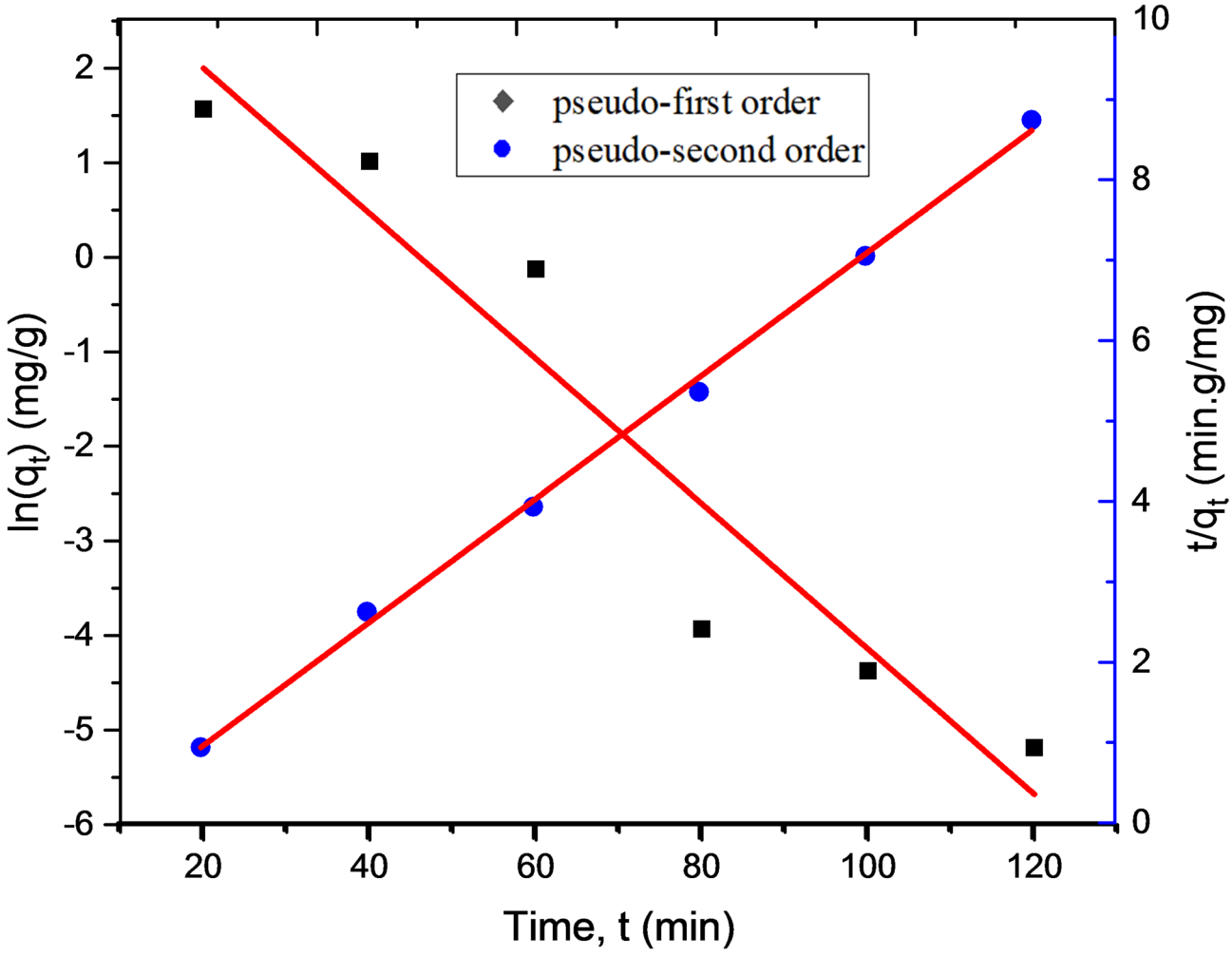

Fig. 13. Adsorption kinetics for adsorption of fluoride using cellulose/Hap nanocomposite.

Temperature, T(K°)	ΔG°(kJ/mol)	ΔH°(kJ/mol)	ΔS°(J/kmol)	R^2
298	-9.60	8.71	0.06	0.97
303	-9.99			
308	-10.23			
313	-10.58			
318	-10.84			

Table 9. Thermodynamic parameters for the fluoride adsorption at various temperatures.

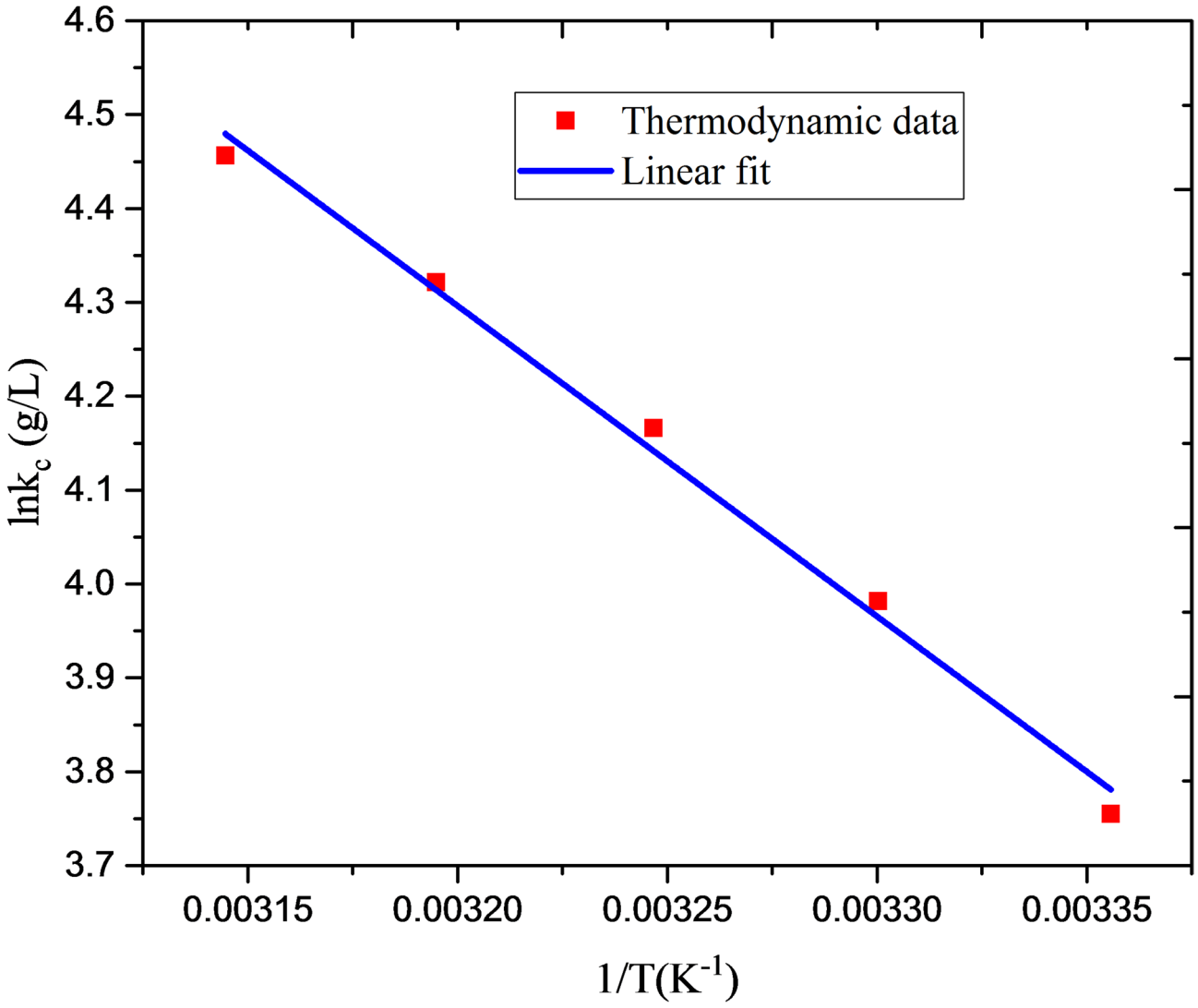

Fig. 14. The plot of $\ln K_c$ verses 1/T on adsorption of fluoride using cellulose/Hap nanocomposite.

(ΔS°) and enthalpy change (ΔH°) were calculated from the intercept and slope, respectively. The high R^2 value of 0.97 and the alignment of data points on the straight line indicate that the thermodynamic models effectively depict the adsorption of fluoride ions on the produced nanocomposite surface. All ΔG° values were negative and decreased with increasing temperature, suggesting that the adsorption of fluoride ions by the cellulose/Hap nanocomposite adsorbent occurs naturally[60]. Reactants possess more free energy than products, indicating that the current adsorption experiment is thermodynamically possible. The positive enthalpy change (ΔH°) of 8.71 kJ/mol demonstrates that the adsorption process of fluoride ions is endothermic. Fluoride adsorption on a cellulose/Hap nanocomposite causes an increase in disorder at the solid/solution interface, as seen by the positive ΔS° value (0.06 J/kmol)[61]. Adsorption does not need additional energy[62]. The study found that changing the temperature from 298 to 318 K had no effect on fluoride removal effectiveness using a synthesized adsorbent. However, in the literature, at 323 K, fluoride adsorption degreases utilizing BCSO, BCSO/$MnFe_2O_4$@La-MOF BCSO/$MnFe_2O_4$ adsorbents, indicating an exothermic reaction with higher fluoride mobility[63]. This indicates that cellulose/Hap nanocomposite adsorbent is stable in 298–318 K temperature ranges.

Regeneration and reusability of adsorbent

The adsorbent regeneration is necessary to minimize costs and the expenses associated with producing new adsorbent[64]. The adsorbed fluoride ions were removed during the regeneration procedure. The adsorbent's regeneration rate was 95.80%. This regeneration outcome was similar to the findings seen in the literature[23]. The adsorbent's reusability was performed under optimal conditions: 1.43 g/L dose, 24.43 mg/L initial concentration, pH 5.24, and 77 min of contact time at 30 °C. The removal efficiencies for each consecutive cycle were 96.85%, 94.03%, 90.45%, 84.71%, and 75.04%, as depicted in Fig. 15. The adsorbent's removal effectiveness decreased throughout each of the five recycling cycles. This might be due to leaching of active cites in the adsorption

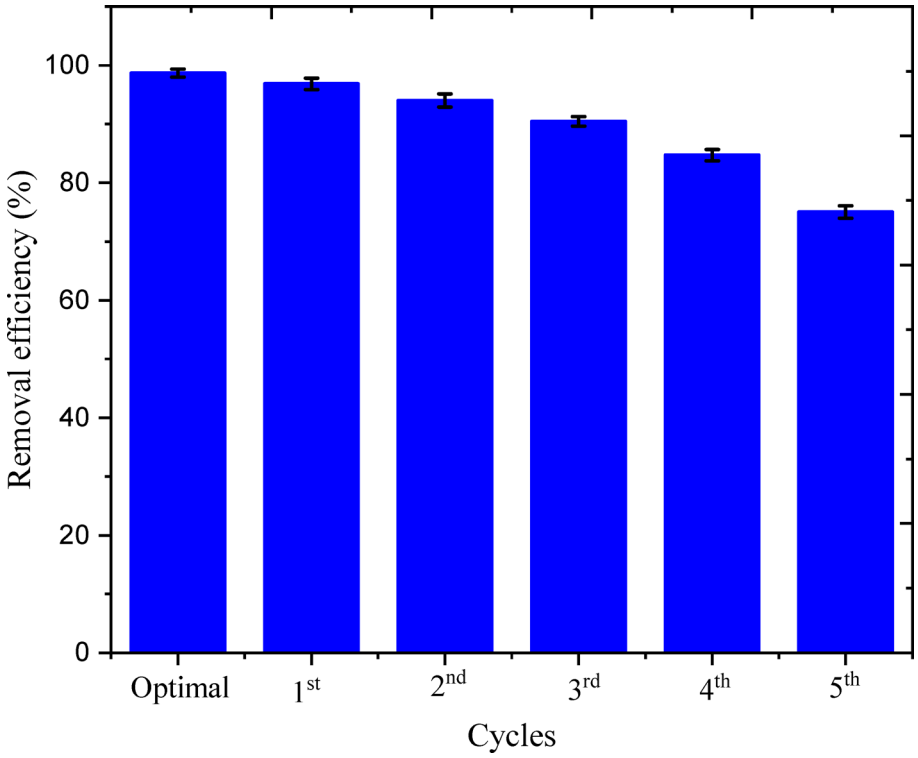

Fig. 15. Fluoride ion removal (%) by regenerated cellulose/Hap nanocomposite adsorbent.

Adsorbents	AC (mg/g)	RE (%)	AD (g/L)	CT (min)	IFC (mg/L)	T (° C)	pH	RR (%)	Ref.
Padina sanctae crucis algae	1.65	97	48	5	8	25 ± 1	7	-	[65]
$MgO@Al_2O_3$	37.35	90	3	480	30	30 ± 2	6.8	-	[66]
Al_2O_3 nanoparticles	13.7	20	0.5	60	30	25 ± 2	5.4	-	[67]
Catla (*Catla catla*)	4.89	98.9	2.29	179.49	8.49	40	9.93	94.3	[46]
activated carbon/aluminum oxide composite	4.10	98	2.0	120	6.0	50	5.9	-	[47]
Cellulose/ HAp nanocomposite	23.02	98.68	1.43	77	24.43	30 ± 1	5.24	95.80	This study

Table 10. Comparative study of optimized conditions of different adsorbents used in fluoride removal. AC- adsorption capacities, Re-removal efficiency, AD- adsorbent dose, CT- contact time, IFC- initial fluoride ion concentration, T- temperature and RR- regeneration rate.

media and reduction of porosity of adsorbent by attachment of adsorbate material. The findings indicate that the adsorbent may be reused for up to three cycles, enhancing its economic viability.

Data on the adsorption of fluoride ions by various adsorbents are collected in Table 10. It presents the following parameters characterizing the adsorption of fluoride ions: the adsorption capacity (AC) and removal efficiency (RE) under optimal conditions for defluridation. The ideal pH value for fluoride removal falls in the range of 5–7. The adsorption experiment employing Padina sanctae-crucis algae as an adsorbent showed limited adsorption capacity despite using a large quantity of adsorbent (48 g/L)[65]. The maximum adsorption capacity was achieved by utilizing $MgO@Al_2O_3$ nanoparticles to remove fluoride ions from water. Nevertheless, a longer contact time (CT) might be expensive[66]. The present study achieved greater AC and RE under optimal conditions compared to previous published data.

Conclusion

Exceeding the WHO-recommended threshold of fluoride in drinking water might adversely affect people's health. Defluoridation is necessary to make water with a high fluoride content safe to drink. The study utilized a newly developed cellulose/HAp nanocomposite for water defluoridation. HAp was synthesized from the shell of a chicken egg, and cellulose was produced from bamboo. The characterization of the new adsorbent indicates that the produced materials have distinct and required properties. Three levels of four essential process variables: dose, pH, contact time, and initial fluoride concentrations were investigated on adsorption process. The optimized conditions were validated with very low standard deviation of 0.71 and a maximum desirability of 1. The highest removal efficiency of 98.68% was attained by employing dosage of 1.43 g/L for 77 min, at a

pH of 5.24, and with an initial concentration of 24.43 mg/L. The fluoride ions adsorption onto the cellulose/Hap nanocomposite can be described by the pseudo-second-order kinetic model and the Langmuir isotherm. Thermodynamic analyses show that the experimental procedure is both spontaneous and endothermic, as confirmed by the positive values of ΔH° and ΔS°, as well as all negative values of ΔG°. According to regeneration and reusability tests, adsorbent can be reused. Concluding, the cellulose/Hap nanocomposite is efficient and an eco-friendly adsorbent for removing fluoride from water, with high removal efficiency under cost-effective operating circumstances.

Data availability

Correspondence and requests for materials should be addressed to S.L.M.

Received: 30 November 2024; Accepted: 24 July 2025
Published online: 06 August 2025

References

1. Keshavarz, M., Foroutan, R., Papari, F., Bulgariu, L. & Esmaeili, H. Synthesis of CaO/Fe2O3 nanocomposite as an efficient nanoadsorbent for the treatment of wastewater containing cr (III). *Sep. Sci. Technol.* **56**, 1328–1341 (2021).
2. Abshirini, Y., Esmaeili, H. & Foroutan, R. Enhancement removal of cr (VI) ion using magnetically modified MgO nanoparticles. *Mater Res. Express* **6**, (2019).
3. Esmaeili, H., Foroutan, R., Jafari, D. & Aghil Rezaei, M. Effect of interfering ions on phosphate removal from aqueous media using magnesium oxide@ferric molybdate nanocomposite. *Korean J. Chem. Eng.* **37**, 804–814 (2020).
4. Savari, A., Hamidi, A., Farjadfard, S., Omidvar, M. & Ramavandi, B. Zirconium-based materials for fluoride removal from aqueous environments: A literature review and scientometric analysis. *Colloids Interface Sci. Commun.* **55**, 100722 (2023).
5. Shaji, E. et al. Fluoride contamination in groundwater: A global review of the status, processes, challenges, and remedial measures. *Geosci. Front.* **15**, 101734 (2024).
6. Malak, K. et al. Author ' s accepted manuscript A review of fluoride in African groundwater and local remediation methods. *Groundw. Sustain. Dev.* https://doi.org/10.1016/j.gsd.2016.09.001 (2016).
7. Savari, A. et al. Physicochemical characteristics and mechanism of fluoride removal using powdered zeolite-zirconium in modes of pulsed& continuous sonication and stirring. *Adv. Powder Technol.* **31**, 3521–3532 (2020).
8. Ren, C., Li, H. H., Zhang, C. Y. & Song, X. C. Effects of chronic fluorosis on the brain. *Ecotoxicol. Environ. Saf.* **244**, 114021 (2022).
9. Wei, W., Pang, S. & Sun, D. The pathogenesis of endemic fluorosis: research progress in the last 5 years. *J. Cell. Mol. Med.* **23**, 2333–2342 (2019).
10. Kumar, P. S. et al. Treatment of fluoride-contaminated water. A review. *Environ. Chem. Lett.* **17**, 1707–1726 (2019).
11. Wan, K. et al. Removal of fluoride from industrial wastewater by using different adsorbents: A review. *Sci. Total Environ.* **773**, 145535 (2021).
12. Yadav, K. K., Gupta, N., Kumar, V., Khan, S. A. & Kumar, A. A review of emerging adsorbents and current demand for defluoridation of water: Bright future in water sustainability. *Environ. Int.* **111**, 80–108 (2018).
13. Khandare, D. & Mukherjee, S. A review of metal oxide nanomaterials for fluoride decontamination from water environment. *Mater. Today Proc.* 18, 1146–1155 (2019).
14. Yapo, N. S. et al. Removal of fluoride in groundwater by adsorption using hydroxyapatite modified corbula trigona shell powder. *Chem Eng. J. Adv* **12**, (2022).
15. George, S., Mehta, D. & Saharan, V. K. Application of hydroxyapatite and its modified forms as adsorbents for water defluoridation: An insight into process synthesis. *Rev. Chem. Eng.* **36**, 369–400 (2020).
16. Mourabet, M. et al. Removal of fluoride from aqueous solution by adsorption on hydroxyapatite (HAp) using response surface methodology. *J. Saudi Chem. Soc.* **19**, 603–615 (2015).
17. Majamo, S. L., Amibo, T. A. & Tsegaw, E. Z. Enhanced cellulose extraction from Agave plant (Agave Americana Species) for synthesis of magnetic/cellulose nanocomposite for defluoridation of water. *Mater. Today Commun.* **38**, 107683 (2024).
18. Phromphithak, S., Tippayawong, N., Onsree, T. & Lauterbach, J. Pretreatment of corncob with green deep eutectic solvent to enhance cellulose accessibility for energy and fuel applications. *Energy Rep.* **8**, 579–585 (2022).
19. Yilmaz, P., Öztürk Er, E., Bakirdere, S., Ülgen, K. & Özbek, B. Application of supercritical gel drying method on fabrication of mechanically improved and biologically safe three-component scaffold composed of graphene oxide/chitosan/hydroxyapatite and characterization studies. *J. Mater. Res. Technol.* **8**, 5201–5216 (2019).
20. Desalegn, Y. M., Andoshe, D. M. & Desissa, T. D. Composite of bentonite/CoFe2O4/hydroxyapatite for adsorption of Pb (II). *Mater. Res. Express*. **7**, 0–16 (2020).
21. Fu, L. H., Qi, C., Liu, Y. J., Cao, W. T. & Ma, M. G. Sonochemical synthesis of cellulose/hydroxyapatite nanocomposites and their application in protein adsorption. *Sci. Rep.* **8**, 1–12 (2018).
22. Yi, X. et al. Highly efficient removal of uranium(VI) from wastewater by polyacrylic acid hydrogels. *RSC Adv.* **7**, 6278–6287 (2017).
23. Mondal, P., Mehta, D. & George, S. Defluoridation studies with synthesized magnesium-incorporated hydroxyapatite and parameter optimization using response surface methodology. **3994**, (2016).
24. Abd El-Fattah, M., Hasan, A. M. A., Keshawy, M., Saeed, E., Aboelenien, O. M. & A. M. & Nanocrystalline cellulose as an eco-friendly reinforcing additive to polyurethane coating for augmented anticorrosive behavior. *Carbohydr. Polym.* **183**, 311–318 (2018).
25. Torstensen, J., Helberg, R. M. L., Deng, L., Gregersen, Ø. W. & Syverud, K. PVA/nanocellulose nanocomposite membranes for CO2 separation from flue gas. *Int. J. Greenh. Gas Control.* **81**, 93–102 (2019).
26. Danaei, M. et al. Impact of particle size and polydispersity index on the clinical applications of lipidic nanocarrier systems. *Pharmaceutics* **10**, 1–17 (2018).
27. Ruan, Z. et al. Synthesis of hydroxyapatite/multi-walled carbon nanotubes for the removal of fluoride ions from solution. *Appl. Surf. Sci.* **412**, 578–590 (2017).
28. Mehta, D., Mondal, P., Saharan, V. K. & George, S. Synthesis of hydroxyapatite nanorods for application in water defluoridation and optimization of process variables: advantage of ultrasonication with precipitation method over conventional method. *Ultrason. Sonochem*. **37**, 56–70 (2017).
29. Bessaies, H. et al. Characterization and physicochemical aspects of novel cellulose-based layered double hydroxide nanocomposite for removal of antimony and fluoride from aqueous solution. *J. Environ. Sci. (China)*. **102**, 301–315 (2021).
30. Damiri, F. et al. Waste sludge from shipping docks as a catalyst to remove amoxicillin in water with hydrogen peroxide and ultrasound. *Ultrason Sonochem* **68**, (2020).
31. Mojahedimotlagh, F. et al. Azithromycin decomposition from simple and complex waters by H2O2 activation over a recyclable catalyst of clay modified with nanofiltration process Brine. *Environ. Technol. Innov.* **33**, 103512 (2024).

32. Majamo, S. L., Amibo, T. A. & Bedru, T. K. Synthesis and application of biomass-derived magnetic Biochar catalyst for simultaneous esterification and trans-esterification of waste cooking oil into biodiesel: modeling and optimization. *Mater. Renew. Sustain. Energy*. **12**, 147–158 (2023).
33. Majamo, S. L. & Amibo, T. A. Modeling and optimization of chemical-treated torrefaction of wheat straw to improve energy density by response surface methodology. *Biomass Convers. Biorefinery*. https://doi.org/10.1007/s13399-023-04192-y (2023).
34. Abdelraof, M. et al. Green synthesis of bioactive Hydroxyapatite / Cellulose composites from food industrial wastes. *J. Inorg. Organomet. Polym. Mater.* **32**, 4614–4626 (2022).
35. Jiang, Q. et al. Halohydrin dehalogenase immobilization in magnetic Biochar for sustainable halocarbon biodegradation and biotransformation. *Environ. Technol. Innov.* **27**, 102759 (2022).
36. Gazińska, M. et al. Influence of hydroxyapatite surface functionalization on thermal and biological properties of poly(L-lactide)- and poly(l-lactide-co-glycolide)-based composites. *Int. J. Mol. Sci.* **21**, 1–21 (2020).
37. Foroutan, R., Mohammadi, R., Taheri, M., Ahmadi, A. & Ramavandi, B. Edible waste oil to biofuel using reclaimable g-C3N4/HAp/Fe3O4/K2CO3 nanobiocomposite catalyst: toxicity evaluation and optimization. *Environ. Technol. Innov.* **32**, 103403 (2023).
38. Foroutan, R. et al. Calcined alluvium of agricultural streams as a recyclable and cleaning tool for cationic dye removal from aqueous media. *Environ. Technol. Innov.* **17**, 100530 (2020).
39. Foroutan, R., Peighambardoust, S. J., Mohammadi, R., Ramavandi, B. & Boffito, D. C. One-pot transesterification of non-edible Moringa Oleifera oil over a MgO/K2CO3/HAp catalyst derived from poultry skeletal waste. *Environ. Technol. Innov.* **21**, 101250 (2021).
40. Fseha, Y. H., Shaheen, J. & Sizirici, B. Phenol contaminated municipal wastewater treatment using date palm frond biochar: optimization using response surface methodology. *Emerg. Contam.* **9**, 100202 (2023).
41. Beyan, S. M., Amibo, T. A., Prabhu, S. V. & Ayalew, A. G. Production of Nanocellulose Crystal Derived from Enset Fiber Using Acid Hydrolysis Coupled with Ultrasonication, Isolation, Statistical Modeling, Optimization, and Characterizations. *J. Nanomater.* (2021). (2021).
42. Kanaujia, S., Singh, B. & Singh, S. K. Removal of Fluoride from Groundwater by Carbonised*Punica granatum* Carbon (CPGC) Bio-Adsorbent. *J. Geosci. Environ. Prot.* 03, 1–9 (2015).
43. Kumari, U., Behera, S. K. & Meikap, B. C. Defluoridation of synthetic and industrial wastewater by using acidic activated alumina adsorbent: characterization and optimization by response surface methodology. *J. Environ. Sci. Heal - Part. Toxic/Hazardous Subst. Environ. Eng.* **54**, 79–88 (2019).
44. Botsa, S. M. & Basavaiah, K. Defluoridation in aqueous solution by a composite of reduced graphene oxide decorated with cuprous oxide via sonochemical. *Arab. J. Chem.* **13**, 7970–7977 (2020).
45. Takdastan, A., Emami Tabar, S., Neisi, A. & Eslami, A. Fluoride removal from drinking water by electrocoagulation using iron and aluminum electrodes. *Jundishapur J. Heal Sci* **6**, (2014).
46. Bhaumik, R., Mondal, N. K. & Chattoraj, S. An optimization study for defluoridation from synthetic fluoride solution using scale of Indian major carp Catla (Catla catla): an unconventional biosorbent. *J. Fluor. Chem.* **195**, 57–69 (2017).
47. Iwar, R. T., Iorhemen, O. T., Ogedengbe, K. & Kayode, K. Environmental chemistry and ecotoxicology novel aluminium (hydr) oxide-functionalized activated carbon derived from Raf Fi a palm (Raphia hookeri) shells: augmentation of its adsorptive properties for Ef Fi Cient Fl Uoride uptake in aqueous media. *Environ. Chem. Ecotoxicol.* **3**, 142–154 (2021).
48. Hashim, K. S. et al. Adsorption of fluoride on a green adsorbent derived from wastepaper: kinetic, isotherm and characterisation study. *Case Stud. Chem. Environ. Eng* **8**, (2023).
49. Mukhlish, M. Z., Bin, Nazibunnesa, S., Islam, S., Mahmood, A. & Uddin, M. T. A. S. Preparation of chemically and thermally modified water caltrop epicarp (Trapa natans L.) adsorbent for enhanced adsorption of Ni(II) from aqueous solution. *Heliyon* **9**, (2023).
50. Kusrini, E. et al. Kinetics, isotherm, thermodynamic and bioperformance of defluoridation of water using praseodymium-modified Chitosan. *J. Environ. Chem. Eng.* **7**, 103498 (2019).
51. Widiartyasari Prihatdini, R., Suratman, A. & Siswanta, D. Linear and nonlinear modeling of kinetics and isotherm of malachite green dye adsorption to trimellitic-modified pineapple peel. *Mater. Today Proc.* 88, 33–40 (2023).
52. Nannu Shankar, S. et al. Adsorption kinetics, equilibrium and thermodynamics of a textile dye V5BN by a natural nanocomplex material: clinoptilolite. *Energy Nexus*. **10**, 100197 (2023).
53. Semwal, N., Mahar, D., Chatti, M., Dandapat, A. & Chandra, M. Heliyon adsorptive removal of congo red dye from its aqueous solution by Ag – Cu – CeO 2 nanocomposites: adsorption kinetics, isotherms, and thermodynamics. *Heliyon* **9**, e22027 (2023).
54. Peighambardoust, S. J. et al. Effectiveness of polyacrylamide-g-gelatin/ACL/Mg-Fe LDH composite hydrogel as an eliminator of crystal Violet dye. *Environ. Res.* **258**, 119428 (2024).
55. Mahdavi, Z. et al. Enhancing fluoride ion removal from aqueous solutions and glass manufacturing wastewater using modified orange Peel Biochar magnetic composite with MIL-53. *Environ. Res.* **262**, 119825 (2024).
56. Ahmadlouydarab, M. & Mohammadi, R. Accepted Manuscript. (2018).
57. Aragaw, T. A. & Alene, A. N. A comparative study of acidic, basic, and reactive dyes adsorption from aqueous solution onto Kaolin adsorbent: effect of operating parameters, isotherms, kinetics, and thermodynamics. *Emerg. Contam.* **8**, 59–74 (2022).
58. WAghmare, S. S. & Arfin, T. Fluoride removal by clays, geomaterials, minerals, low cost materials and zeolites by adsorption: A review. *Int. J. Sci. Eng. Technol. Res.* **4**, 3663–3676 (2015).
59. Abumelha, H. M. et al. Evaluation of Tetracycline removal by magnetic metal organic framework from aqueous solutions: adsorption isotherm, kinetics, thermodynamics, and Box-Behnken design optimization. *J. Saudi Chem. Soc.* **27**, 101706 (2023).
60. Ahmad, N. et al. Insight into the adsorption thermodynamics, kinetics, and photocatalytic studies of polyaniline/SnS2 nanocomposite for dye removal. *J. Hazard. Mater. Adv.* **10**, 100321 (2023).
61. Qais, D. S. et al. Nano-zinc oxide fibers: synthesis, characterization, adsorption of acid blue 92 dye, isotherms, thermodynamics and kinetics. *Emerg Contam* **9**, (2023).
62. Zuhara, S., Pradhan, S. & McKay, G. Investigating mixed biosolids and cardboard for methylene blue adsorption: activation, adsorption modelling and thermodynamics. *Environ. Res.* **225**, 115534 (2023).
63. Foroutan, R., Mohammadi, R., Razeghi, J., Ahmadi, M. & Ramavandi, B. Amendment of sargassum oligocystum bio-char with MnFe2O4 and lanthanum MOF obtained from PET waste for fluoride removal: A comparative study. *Environ. Res.* **251**, 118641 (2024).
64. He, Y. et al. Enhanced fluoride removal from water by rare Earth (La and Ce) modified alumina: adsorption isotherms, kinetics, thermodynamics and mechanism. *Sci. Total Environ.* **688**, 184–198 (2019).
65. Dobaradaran, S. et al. Biosorption of fluoride from aqueous phase onto Padina sanctae crucis algae: Evaluation of biosorption kinetics and isotherms. *Desalin. Water Treat.* **57**, 28405–28416 (2016).
66. Dayananda, D. et al. Synthesis of MgO nanoparticle loaded mesoporous al 2 O 3 and its defluoridation study. *Appl. Surf. Sci.* **329**, 1–10 (2015).
67. Hafshejani, L. D. et al. Optimization of fluoride removal from aqueous solution by Al2O3 nanoparticles. *J. Mol. Liq.* **238**, 254–262 (2017).

Acknowledgements

The authors would like to acknowledge Jimma Institute of Technology (JIT) center of excellence for partial

support for this research.

Author contributions

CRediT authorship contribution statement: T.A.A.: Conceptualization, Data curation, Formal analysis, Investigation, Visualization, Writing – original draft and Writing – review & editing. S.L.M.: Conceptualization, Data curation, Formal analysis, Investigation, Methodology, Visualization, Writing – original draft and Writing – review & editing. B.M.G.: Formal analysis, Methodology, VisualizationWriting – original draft and Writing – review & editing. D.K-Ł.: Data curation, Formal analysis, Investigation, Methodology, Supervision, Validation, Visualization and Writing – review & editing.

Declarations

Competing interests

The authors declare no competing interests.

Additional information

Correspondence and requests for materials should be addressed to S.L.M.

Reprints and permissions information is available at www.nature.com/reprints.

Publisher's note Springer Nature remains neutral with regard to jurisdictional claims in published maps and institutional affiliations.